

Chapter 9

SHORT WAVELENGTH INTERMEDIATE FREQUENCY TYRE MODEL

9.1. Introduction

In Chapter 5 the stretched string model, possibly featuring tread elements and tyre inertia, was used to study the dynamic response of the side force and aligning torque to lateral, vertical and yaw motion variations of the wheel axle. These motions, however, had to be restricted in magnitude to allow the theory to remain linear. Several approximations were introduced to simplify the model description which made it possible to consider ranges of relatively large slip through a simple non-linear extension. The limitation, however, was that only relatively large wavelength phenomena ($> \text{ca. } 1.5 \text{ m}$) could be investigated with these simplified models.

The present chapter describes a model that is able to cover situations where the wavelength is relatively short ($> \text{ca. } 10 \text{ cm}$ and even shorter for modelling road obstacle enveloping properties), the frequency is relatively high ($< 60\text{-}80 \text{ Hz}$) while the level of slip can be high. Situations in which combined slip occurs can be handled and the *Magic Formula* model can be used as the basis for the non-linear force and moment description. As a result, a continuous transition from time varying slip situations to steady-state conditions is realised. The original model development was restricted to the more important responses to variations of longitudinal and side slip. Also, the possibility to traverse distinct road irregularities (cleats) was included in the tyre model. The model is based on the work of Zegelaar (1998) and Maurice (2000) conducted at the Delft University of Technology and supported by TNO Automotive and a consortium of industries. The model is referred to as the *SWIFT* model (corresponding to the title of the present chapter). Subsequent developments of the model made it possible to also include variations of camber and turn slip.

The crucial step that was taken to reach further than one can by using the string model is the separation of modelling the carcass and the contact patch. In this way a much more versatile model can be established that correctly describes slip properties at short wavelengths and at high levels of slip. The model

achieved can be seen as a further development of the enhanced single contact point model of Section 7.3, Fig.7.15. Five elements of the model structure can be distinguished: (1) The inertia of the belt that has been taken into account to properly describe the dynamics of the tyre. The restriction to frequencies of about 60Hz allows the belt to be considered as a rigid circular ring. (2) The so-called residual stiffnesses that has been introduced between contact patch and ring to ensure that the total static tyre stiffnesses in vertical, longitudinal, lateral and yaw directions are correct. The total tyre model compliance is made up of the carcass compliance, the residual compliance (in reality a part of the total carcass compliance) and the tread compliance. (3) The brush model that represents the contact patch featuring horizontal tread element compliance and partial sliding. On the basis of this model, the effects of the finite length and width of the footprint are approximately included. This element of the model is the most complex part and accomplishes the reduction of the allowed input wavelength to ca. 10cm. (4) Effective road inputs to enable the simulation of the tyre moving over an uneven road surface with the enveloping behaviour of the tyre properly represented. The actual three-dimensional profile of the road is replaced by a set of four effective inputs: the effective height, the effective forward and transverse slopes of the road plane and the effective forward road curvature that is largely responsible for the variation of the tyre effective rolling radius. (5) The *Magic Formula* tyre model to describe the non-linear slip force and moment properties. In Fig.9.1 the model structure has been depicted.

Similar more physically oriented models have been developed. A notable example is the *BRIT* model of Gipser. He employs a brush-ring model featuring

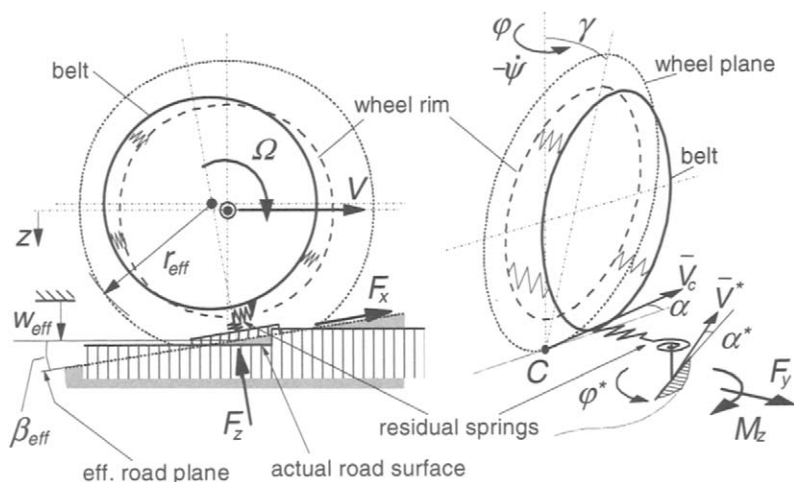


Fig. 9.1. General configuration of the *SWIFT* model featuring rigid belt ring, residual stiffnesses, contact patch slip model and effective road inputs.

tread elements distributed over a finite contact patch with realistic pressure distributions and demonstrates the use of the model with simulations of the tyre traversing a sinusoidal road surface also at a slip angle and at braking, cf. Gipser et al. (1997). Other models: *FTire* and *RMOD-K*, have been developed by Gipser (1999) and Oertel and Fandre (1999) respectively. In Section 9.6 a comparative outline of these two models and of the *SWIFT* model is presented.

In the ensuing theoretical treatment, first, in Section 9.2, the slip model of the contact patch covering small wavelengths and large slip will be dealt with. Secondly, the model for the description of the dynamic behaviour of the rigid belt ring will be added, Sec.9.3. Thirdly, the feature of the model that takes care of running over uneven roads will be addressed, Chapter 10. Full scale tyre test results will demonstrate the validity of the model.

9.2. The Contact Patch Slip Model

In this section, we will first represent the contact patch with tread elements by the brush model. Because of its relative complexity, the analytical model that describes the non-steady-state response to slip variations is approximated by a set of first-order differential equations. This contact model is tested by attaching the base line of the brush model to the wheel plane through a compliant carcass. For reasons of practical use, we finally introduce the *Magic Formula* to handle the non-linear behaviour of the model.

9.2.1. Brush Model Non-Steady-State Behaviour

The steady-state characteristics of the model have been discussed in Chapter 3. As a first step, we will derive the equations that govern the response of the forces and moment to small variations of the wheel slip with respect to a given level of wheel slip indicated with subscript o .

Longitudinal Slip

For the case of pure longitudinal slip κ_{co} of the contact patch, the point of transition from adhesion to sliding is located according to Eq.(3.44) with (3.34,3.40) at a distance x_t from the contact centre:

$$x_t = a \left(\frac{2\theta|\kappa_{co}|}{1 + \kappa_{co}} - 1 \right) \quad (9.1)$$

The composite parameter θ has been defined in Chapter 3, Eq.(3.46). The length of the adhesion range $2am=a-x$, that begins at the leading edge is characterised by the fraction m that in the present chapter replaces the symbol λ to avoid confusion with the notation for the wavelength. We have:

$$m = 1 - \theta \frac{|\kappa_{co}|}{1 + \kappa_{co}} \quad \text{if} \quad \frac{|\kappa_{co}|}{1 + \kappa_{co}} < \frac{1}{\theta} \quad \text{else} \quad m = 0 \quad (9.2)$$

An important observation is that at small variations of slip we may assume that only in the adhesion range changes in deflection occur.

For the development of the transient model we start out from the basic rolling contact differential equations (2.55,2.56). In the adhesion range we find for the longitudinal tread element deflection u_c in the case that only longitudinal slip is considered:

$$\frac{\partial \tilde{u}_c}{\partial t} - V_{ro} \frac{\partial \tilde{u}_c}{\partial x} = \tilde{V}_{sxc} = -V_{xco} \tilde{\kappa}_c \quad (9.3)$$

Where the tilde designates the variation with respect to the steady-state level. The average linear speed of rolling of the contact patch is equal to that of the wheel rim and reads:

$$V_{ro} = V_{ro} = V_x - V_{sxo} = V_x (1 + \kappa_{co}) \quad (9.4)$$

The Fourier transform of the deflection becomes with U and K denoting the transformed quantities of u and κ respectively and ω_s the path frequency:

$$\tilde{U}_c = \frac{1}{i\omega_s} \left(1 - e^{-i\omega_s(a-x)V_x/V_{ro}} \right) \tilde{K}_c \quad (9.5)$$

Here, the boundary condition which says that the deflection vanishes at the leading edge is satisfied. By integrating over the range of adhesion and multiplying with the tread element stiffness c_p the frequency response function of the variation of F_x to the variation of κ_c is obtained. With the reduced frequency

$$\omega'_s = \frac{m\omega_s}{1 + \kappa_{co}} \quad (9.6)$$

and the local derivative of F_x to κ_c

$$C_{F\kappa c} = \frac{2c_p m^2 a^2}{1 + \kappa_{co}} \quad \text{if} \quad \frac{|\kappa_{co}|}{1 + \kappa_{co}} < \frac{1}{\theta} \quad \text{else} \quad C_{F\kappa c} = 0 \quad (9.7)$$

the expression for the response function becomes when still adhesion occurs in the contact patch (first condition of (9.2)):

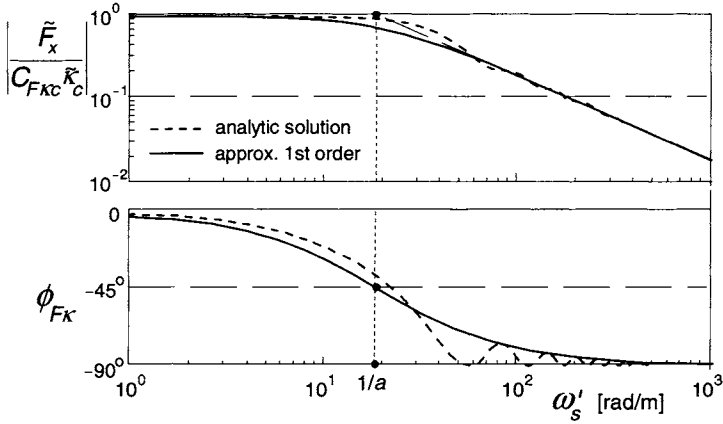


Fig. 9.2. Frequency response function of the longitudinal force variation to longitudinal slip variation of the brush model versus reduced path frequency according to the exact analytical solution and that of an approximate substitute first-order system at a given level of longitudinal slip.

$$H_{F,\kappa c}(i\omega'_s) = \frac{C_{F\kappa c}}{i\omega'_s a} \left\{ 1 - \frac{1}{2i\omega'_s a} (1 - e^{-2i\omega'_s a}) \right\} \quad (9.8)$$

In Fig.9.2 the resulting amplitude and phase characteristics have been shown together with those of an approximate first-order system. Especially the phase curve appears to exhibit a wavy pattern in the higher frequency range. These waves are considerably attenuated when the contact model is incorporated in a more complete tyre model including carcass compliance as will be shown below.

The first-order substitute model has a frequency response function that reads:

$$H_{F,\kappa c}(i\omega'_s) = \frac{C_{F\kappa c}}{1 + i\omega'_s a} = \frac{C_{F\kappa c}}{1 + i\omega'_s \sigma_c} \quad (9.9)$$

The approximation shows the same high frequency asymptote and steady-state level as the exact model. Apparently, the actual cut-off path frequency reads:

$$\omega_{s,c-o} = \frac{1 + \kappa_{co}}{ma} \quad (9.10)$$

that, obviously, reduces to $1/a$ when the average slip κ_{co} vanishes and as a consequence m (9.2) becomes equal to unity. When the average slip is chosen larger, the length of the adhesion range decreases and the cut-off frequency becomes higher. The relaxation length of the approximate contact model reads according to Eq.(9.9) with (9.6):

$$\sigma_c = \frac{ma}{1 + \kappa_{co}} \quad (9.11)$$

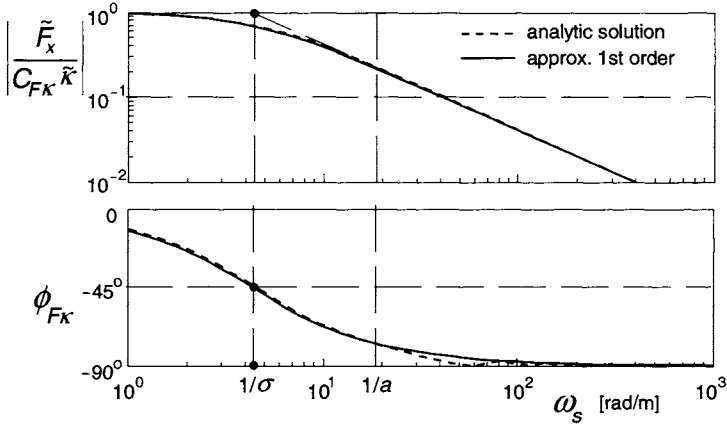


Fig. 9.3. Frequency response function of the longitudinal force variation to longitudinal slip variation of the brush model attached to a flexible carcass versus path frequency according to the exact analytical solution and that of the approximate first-order system at zero longitudinal slip.

which reduces to zero when total sliding occurs.

The performance of the first-order system is reasonable but appears to improve when the filtering action of the carcass compliance is taken into account. In that configuration we have the wheel slip velocity V_{sx} that acts as the input quantity. Adding the time rate of change of the carcass deflection produces the slip velocity of the brush model. The carcass deflection u equals (with fore and aft carcass stiffness c_x introduced):

$$u = \frac{F_x}{c_x} \quad (9.12)$$

The feed-back loop in the augmented system apparently contains a gain equal to $i\omega_s/c_x$. The resulting complete frequency response function reads:

$$H_{F,\kappa}(i\omega_s) = \frac{H_{F,\kappa c}(i\omega_s)}{1 + H_{F,\kappa c}(i\omega_s)i\omega_s/c_x} \quad (9.13)$$

When the approximate first-order system is employed for the contact model, the frequency response function for the complete model becomes using (9.13) with (9.9):

$$H_{F,\kappa}(i\omega_s) = \frac{C_{F\kappa c}}{1 + i\omega_s \sigma} \quad (9.14)$$

where the total relaxation length has been introduced which apparently reads:

$$\sigma = \sigma_c + \frac{C_{F\kappa c}}{c_x} = am + \frac{C_{F\kappa}}{c_x} \quad (9.15)$$

The local longitudinal slip stiffness of the contact patch is here equal to the local longitudinal slip stiffness of the complete model which obviously is due to the assumed inextensibility of the base line of the brush model. So we have at steady state:

$$\frac{\partial F_x}{\partial \kappa} = C_{F\kappa} = C_{F\kappa c} \quad (9.16)$$

At vanishing slip we will add a subscript 0. When total sliding occurs, both σ_c and $C_{F\kappa}$ reduce to zero and the total relaxation length σ vanishes.

Figure 9.3 presents the frequency response function for the total model at vanishing slip, $\kappa_0 = 0$. It is noted that compared with the curves of Fig.9.2 the wavy pattern is considerably reduced. The approximate system performs very well. A wavelength of 10cm occurs at the path frequency $\omega_s = \text{ca. } 60 \text{ rad/m}$.

The differential equation that governs the transient slip response of the contact patch and through that the longitudinal force response, becomes for the approximate system:

$$\sigma_c \frac{d\tilde{\kappa}'_c}{dt} + |V_x| \tilde{\kappa}'_c = |V_x| \tilde{\kappa}_c = -\tilde{V}_{sxc} \quad (9.17)$$

The variation of the force becomes:

$$\tilde{F}_x = C_{F\kappa c} \tilde{\kappa}'_c \quad (9.18)$$

The structure of Eq.(9.17) corresponds with that of Eq.(7.37) of Chapter 7. The response, however, is insensitive to load variations but shows a nice behaviour. The transient response to load variations is sufficiently taken care of through the effect of carcass compliance. As a result, the relaxation length for the response to load variations becomes equal to $C_{F\kappa c}/c_x$ which is somewhat smaller than σ (9.15) that holds for the response to slip variations.

When the average steady-state relation for the longitudinal slip

$$|V_x| \kappa_{co} = -V_{sxc} \quad (9.19)$$

is added to Eq.(9.18) the equation for the total transient slip is obtained:

$$\sigma_c \frac{d\kappa'_c}{dt} + |V_x| \kappa'_c = |V_x| \kappa_c = -V_{sxc} \quad (9.20)$$

that completely corresponds to Eq.(7.54) of the enhanced non-linear transient tyre model. The transient slip κ'_c is subsequently used as input into the steady-state longitudinal force characteristic as will be explained later on and has already been indicated in Chap.7, Sec.7.3.

Lateral Slip

The lateral slip condition is more complex to handle because we have to deal with both the side force and the aligning torque. In addition, in the test condition, the carcass is allowed to not only deflect in lateral direction but also about the vertical axis. This is in accordance with the ultimate *SWIFT* configuration. The connected turn slip behaviour of the contact patch will be dealt with further on.

As with the longitudinal model development, first, the analytic response functions of the brush model will be assessed, in this case to side slip variations. Equation (2.56) gives rise to the following equation for the lateral tread deflection variations:

$$\frac{\partial \tilde{v}_c}{\partial t} - V_{rc0} \frac{\partial \tilde{v}_c}{\partial x} = \tilde{V}_{syc} = -V_{xco} \tilde{\alpha}_c \quad (9.21)$$

Note that for the sake of simplification in the present chapter the notation $\tan \alpha$ is replaced by α , with or without subscript. Similar as for the longitudinal deflection we find for the Fourier transform V_c of the lateral deflection responding to slip angle variations, A_c denoting the brush model slip angle's transform (or actually of $\tan \alpha_c$):

$$\tilde{V}_c = \frac{1}{i\omega_s} \left(1 - e^{-i\omega_s(a-x)V_x/V_{rc0}} \right) \tilde{A}_c \quad (9.22)$$

Again, the responses to variations of the side slip only occur in the range of adhesion. The transition point from adhesion to sliding now occurs at:

$$x_t = a \left(2\theta |\alpha_{co}| - 1 \right) \quad (9.23)$$

and the corresponding adhesion fraction becomes, cf. Eq.(3.8):

$$m = 1 - \theta |\alpha_{co}| \quad \text{if } |\alpha_{co}| < \frac{1}{\theta} \quad \text{else } m = 0 \quad (9.24)$$

As the slip angle of the contact patch remains small in the range where adhesion still occurs, $\cos \alpha_{co}$ has been replaced by unity. By integration of the transformed deflection over the range of adhesion the frequency response functions of the force and the moment variations are established. They read at pure lateral slip ($V_{rc0} = V_x$):

$$H_{F,ac}(i\omega_s) = \frac{C_{Fac}}{i\omega_s am} \left\{ 1 - \frac{1}{2i\omega_s am} \left(1 - e^{-2i\omega_s am} \right) \right\} \quad (9.25)$$

and

$$H_{M,ac}(i\omega_s) = \frac{c_p}{i\omega_s} \left\{ -\frac{1}{\omega_s^2} \left(1 - e^{-2i\omega_s am} \right) + \right. \\ \left. - \frac{a}{i\omega_s} \left(1 + (2m-1)e^{-2i\omega_s am} \right) + 2a^2 m(1-m) \right\} \quad (9.26)$$

The local slope of the steady-state side force characteristic of the brush model is given by:

$$C_{Fac} = 2c_p m^2 a^2 \quad \text{if } |\alpha_{co}| < \frac{1}{\theta} \quad \text{else } C_{Fac} = 0 \quad (9.27)$$

The normalised response function of the side force is identical to that of the longitudinal force if the factor $1+\kappa_{co}$ is omitted in (9.6). The approximate first-order description with response function

$$H_{F,ac}(i\omega_s) = \frac{C_{Fac}}{1 + i\omega_s \sigma_c} \quad (9.28)$$

where

$$\sigma_c = am \quad (9.29)$$

shows the same very good agreement with the exact result as assessed with the longitudinal force response. Similarly we have the differential equation for the variation of the transient side slip:

$$\sigma_c \frac{d\tilde{\alpha}'_c}{dt} + |V_x| \tilde{\alpha}'_c = |V_x| \tilde{\alpha}_c = -\tilde{V}_{syc} \quad (9.30)$$

The variation of the side force becomes:

$$\tilde{F}_y = C_{Fac} \tilde{\alpha}'_c \quad (9.31)$$

After adding the steady-state equation

$$|V_x| \alpha_{co} = -V_{syc} \quad (9.32)$$

to Eq.(9.30), the equation for the total transient side slip is obtained:

$$\sigma_c \frac{d\alpha'_c}{dt} + |V_x| \alpha'_c = |V_x| \alpha_c = -V_{syc} \quad (9.33)$$

As before, the resulting α'_c is used as the input of the steady-state side force function.

We may follow the same procedure to assess the aligning torque equations as was done in Sec.7.3. The resulting first-order response, however, does not always agree with the analytically found tendency. The phase lag and the slope of the high frequency amplitude asymptote indicate that a second-order

behaviour prevails at zero average slip angle while at larger slip angles the response gradually changes into a first-order nature. Apparently, the mechanism is more complex and we should account for the transient response of the pneumatic trail. The variation of the aligning torque may be written as follows:

$$\tilde{M}_z = -t_{co} \tilde{F}_y - \tilde{t}_c F_{yo} \quad (9.34)$$

The analysis conducted by Maurice (2000) shows that the analytically assessed response function of the pneumatic trail variation to slip angle variations can be approximated by the first-order system (9.33) and a so-called phase leading network in series. The frequency response function of the latter reads:

$$H_p(i\omega_s) = C_{tac} \frac{1 + i\omega_s \sigma_1}{1 + i\omega_s \sigma_2} \quad (9.35)$$

The factor in this formula represents the local slope of pneumatic trail characteristic:

$$C_{tac} = \frac{\partial t_c}{\partial \alpha_c} \quad (9.36)$$

which, apparently, is a negative quantity. According to Maurice, adequate values for the parameters σ_1 and σ_2 can be obtained through the formulae:

$$\sigma_2 = \frac{1}{3} a (1 - \theta |\alpha_{co}|) \quad (9.37)$$

or alternatively:

$$\sigma_2 = t_c \quad (9.38)$$

and

$$\frac{\sigma_1}{\sigma_2} = \frac{1}{1 - m^2} \quad (9.39)$$

The block diagram of the current system governed by the equations (9.28,9.34,9.35) is presented in the upper diagram of Fig.9.4. The lower diagram shows an alternative structure of the same system, thereby displaying the extra moment ΔM_z which is governed by the ratio of parameters (9.39). This ratio tends to infinity when full adhesion occurs. Then, $m=1$ and $\alpha_{co}=0$ as becomes clear from Eq.(9.24). The singularity involved has been circumvented by Maurice through the introduction of a function that limits the value of (9.39) around zero lateral slip, $\alpha_{co}=0$. This, however, will slightly disturb the proper response at zero slip angle and thus degrades the linear analysis around zero slip. An alternative way of avoiding the singularity, which obviously is caused by the fact that we actually may have a moment without the simultaneous presence of

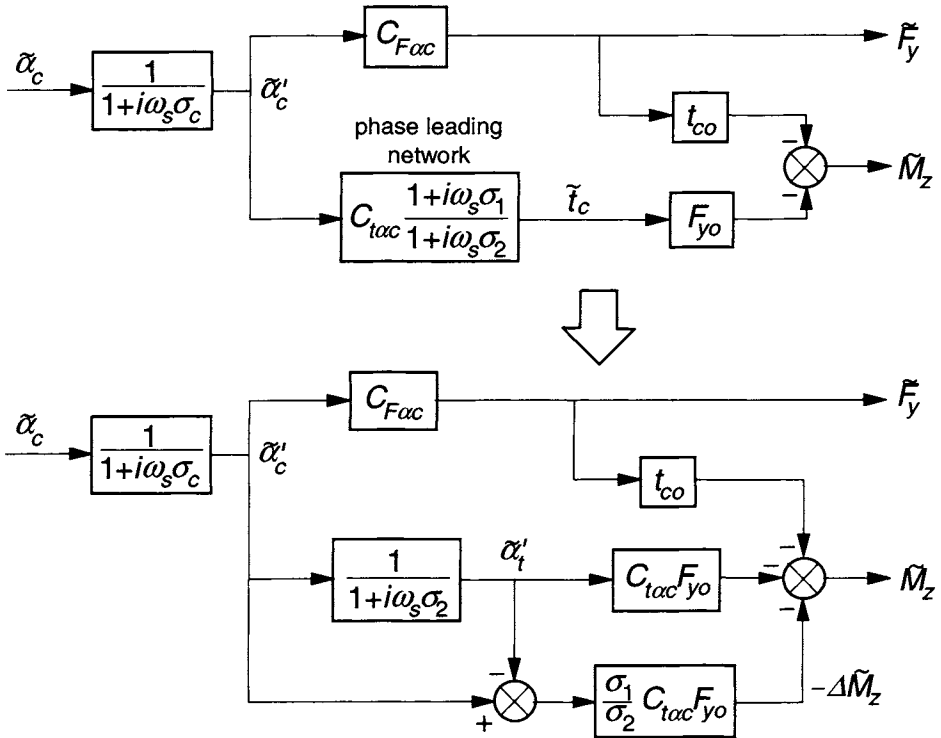


Fig. 9.4. Block diagram of the contact patch model to generate short wavelength transient responses of the side force and the aligning torque to small slip angle variations. The original upper diagram can be replaced by the lower diagram, thereby avoiding singularity at zero slip.

a force, is the consideration of the extra transient moment ΔM_z . This moment is obtained by multiplication of the difference of the transient slip quantities for the force and for the pneumatic trail with three factors the combination of which may be designated with $C_{\Delta M}$:

$$C_{\Delta M} = -\frac{\sigma_1}{\sigma_2} C_{tac} F_{yo} \quad (9.40)$$

It turns out that now the singularity does not show up because both F_{yo} and $1/\sigma_1$ become zero at the same time. This indicates that indeed a moment may arise although at that instant of time the side force is zero. After writing out the factors in (9.40) by using expressions for the side force (3.11), the pneumatic trail (3.13) and further (9.36, 9.39) while in (3.11) λ is replaced by m and $\theta_y \sigma_y$ by $\theta_{\alpha_{co}} = z$ we find for $C_{\Delta M}$:

$$C_{\Delta M} = \frac{1}{3} a C_{Fac0} \xi = C_{Mac0} \xi \quad (9.41)$$

where C_{Mac0} denotes the aligning stiffness of the brush model at zero slip angle and the non-dimensional factor ξ is introduced:

$$\xi = \frac{(1-z)^2}{2-z} \left\{ 3 - \frac{(1-z)(1-2z/3)}{1-z+z^2/3} \right\} \quad \text{if } z < 1 \quad \text{else } \xi = 0 \quad (9.42)$$

with

$$z = \theta |\alpha_{c0}| \quad (9.43)$$

Evaluation of (9.42) reveals that for $z < 1$ the factor ξ may possibly be approximated by

$$\xi \approx 1 - z \quad (9.44)$$

This approximation will be introduced later on when we will deal with the application of the *Magic Formula*.

The differential equations that apply for the contact patch model subjected to small side slip variations with respect to a given side slip level now read:

$$\sigma_c \frac{d\tilde{\alpha}'_c}{dt} + |V_x| \tilde{\alpha}'_c = |V_x| \tilde{\alpha}'_c = -\tilde{V}_{syc} \quad (9.45)$$

$$\sigma_2 \frac{d\tilde{\alpha}'_t}{dt} + |V_x| \tilde{\alpha}'_t = |V_x| \tilde{\alpha}'_c \quad (9.46)$$

from which the variation of the force and moment result:

$$\tilde{F}_y = C_{Fac} \tilde{\alpha}'_c \quad (9.47)$$

$$\tilde{M}_z = -t_{co} \tilde{F}_y - C_{tac} \tilde{\alpha}'_t F_{y0} + C_{\Delta M} (\tilde{\alpha}'_c - \tilde{\alpha}'_t) \quad (9.48)$$

It is of importance to check the step responses to side slip starting from zero slip angle especially right after the start of the step change. Initially we have all variables equal to zero while the slip angle input has reached the new value α_{c0} . The various time derivatives become:

$$\begin{aligned} (t = 0: \quad \alpha_c = \alpha_{c0}, \quad \alpha'_c = \alpha'_t = 0, \quad F_y = M_z = 0) \\ \frac{d\alpha'_c}{dt} = \frac{1}{\sigma_{c0}} |V_x| \alpha_{c0}, \quad \frac{d\alpha'_t}{dt} = 0 \\ \frac{dF_y}{dt} = \frac{|V_x|}{\sigma_{c0}} C_{Fac0} \alpha_{c0}, \quad \frac{dM_z}{dt} = -t_{c0} \frac{dF_y}{dt} + C_{\Delta M0} \frac{d\alpha'_c}{dt} = 0 \end{aligned} \quad (9.49)$$

These results are correct. The last equation holds indeed because we have at

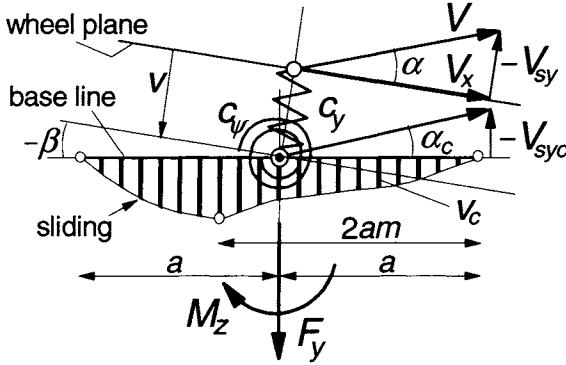


Fig. 9.5. The brush model attached to a carcass possessing lateral and torsional compliance.

vanishing slip angle according to Eq.(9.42): $\xi=1$ and consequently $C_{\Delta M}=t_{c0}C_{Fac0}$ where $t_{c0}=a/3$. Evidently, the extra moment is responsible for the proper start of the course of the aligning torque showing zero slope. This property has been ascertained to occur both in reality and with models, cf. Figs.5.10 and 5.11. Also the response to a lateral wheel displacement $y = \int V_{sy} dt$ at zero forward speed develops correctly. We find with Eq.(7.6) for the force: $F_y = -C_{Fy}y$ and for the moment: $M_z = 0$.

The equations may now further be appraised by first introducing tyre carcass lateral and torsional compliance as depicted in Fig.9.5 and in the corresponding block diagram of Fig.9.6, and subsequently comparing the results with analytical solutions obtained by using Eqs.(9.25,9.26).

As a reference, the steady-state characteristics of the model have been presented in Fig.9.7. The diagram contains the curves for both the complete model and for the brush model alone. It is of interest to note the lower cornering stiffness due to the introduction of carcass compliance. The expression for the lower side slip stiffness can be found to read:

$$C_{Fa} = \frac{c_{\psi}}{c_{\psi} + C_{Mac}} C_{Fac} \quad (9.50)$$

The relaxation length of the complete model found from the cut-off frequency of the side force response function turns out to become:

$$\sigma = \frac{c_{\psi}}{c_{\psi} + C_{Mac}} \left(am + \frac{C_{Fac}}{c_y} \right) = \frac{c_{\psi}}{c_{\psi} + C_{Mac}} am + \frac{C_{Fa}}{c_y} \quad (9.51)$$

The way the relaxation length changes with slip angle is depicted in the right-hand diagram of Fig.9.7. As one might expect, we find that this length multiplied with the increment in wheel slip angle is equal to the increase of the sum of carcass lateral deflection and the average deflection of the adhering tread

refer to the side force response shows the sideways ‘shift’ of the phase lag curves which is caused by the drop in relaxation length with increasing average slip angle. The diagram for the aligning torque response clearly shows the transition from second to first-order behaviour when the average slip angle changes from zero to larger values.

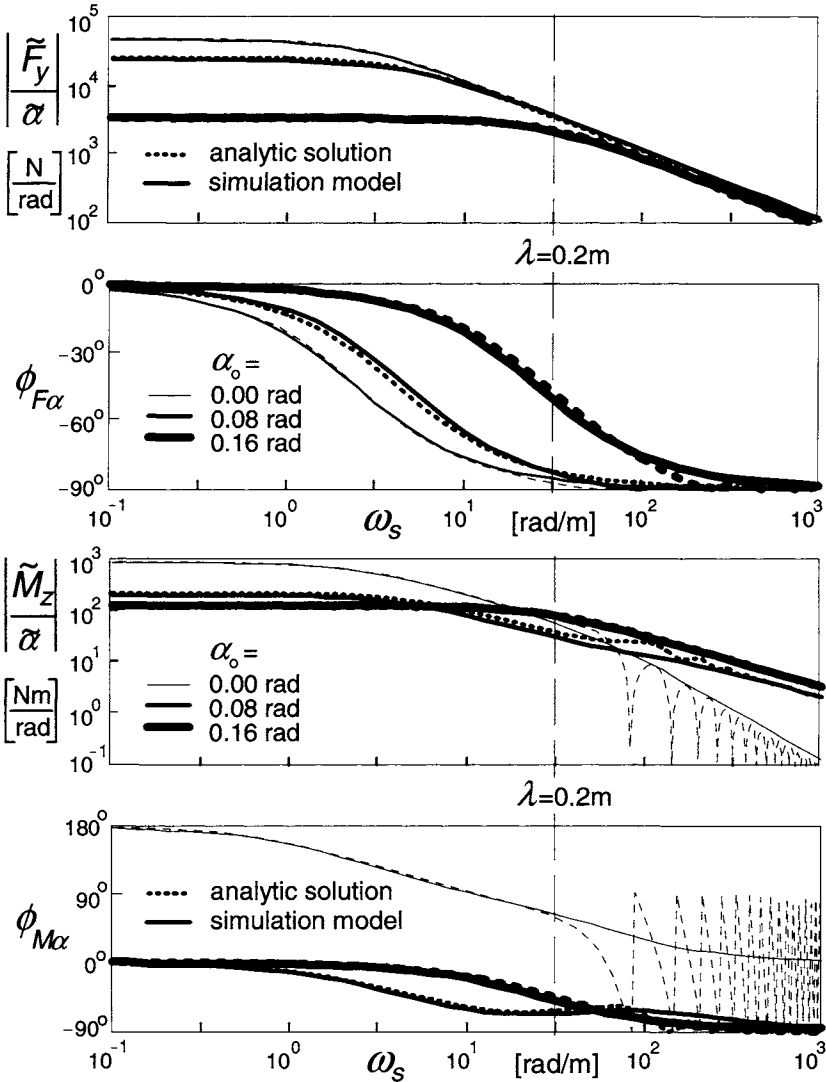


Fig. 9.8. Frequency response functions of linearised system including carcass flexibility at different average slip angle levels according to the analytical solution and to the approximate simulation model. The path frequency at a wavelength of the input wheel plane motion equal to 20cm has been indicated.

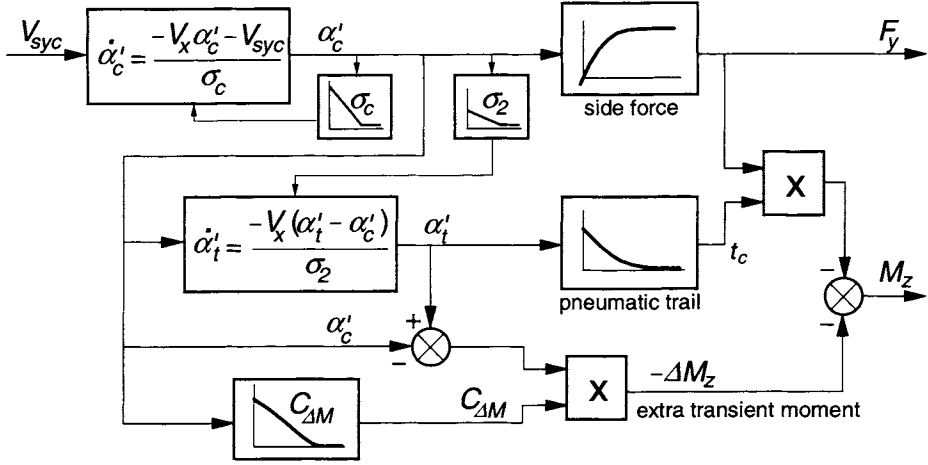


Fig. 9.9. Block diagram of the non-linear model of the contact patch (tread) also valid for larger slip angle variations.

The Eqs.(9.45-48) can be made applicable to the general case of large slip angle variations by adding to (9.45,9.46) the steady-state relations and by rewriting the Eqs.(9.47,9.48) in complete non-linear form so that, when considering a small variation, the linearised equations are recovered. We obtain for the transient slip quantities:

$$\sigma_c \frac{d\alpha'_c}{dt} + |V_x| \alpha'_c = |V_x| \alpha_c = -V_{syc} \quad (9.52)$$

$$\sigma_2 \frac{d\alpha'_t}{dt} + |V_x| \alpha'_t = |V_x| \alpha'_c \quad (9.53)$$

and for the force and moment:

$$F_y = F_y(\alpha'_c) \quad (9.54)$$

$$M_z = -t_c(\alpha'_t) F_y + C_{\Delta M}(\alpha'_c - \alpha'_t) \quad (9.55)$$

The last term representing the extra moment is left in linearised form. This term may be replaced by the difference of two equal functions the derivative of which equals $C_{\Delta M}$, one with argument α'_c and the other with α'_t . Because of the fact that the difference of these two arguments remains small, the linearised version is expected to be sufficiently accurate. The block diagram of the non-linear system displayed in Fig.9.9 may further clarify the structure of the model.

To ensure that the above equations correctly describe the response to large slip angle variations, the simulation model results have been compared with the response of a physical model. That model features a finite number of tread

elements attached to a straight base line. The deflections of carcass and elements are computed at each time step in which the wheel is rolled further over a distance equal to the interval between two successive tread elements and is moved sideways according to the current value of the input slip angle. The actual model employed contains 20 elements. The parameter values used in both models have been listed in Table 9.1.

The slip angle variation is sinusoidal around a given average level. To cover a broad range of operation the computations have been conducted at three wavelengths: $\lambda = 0.2, 1$ and 5m , two average slip angle levels: $\alpha_0 = 0$ and 0.08rad and one amplitude: $\hat{\alpha} = 0.08\text{rad}$.

Table 9.1. Parameter values used for brush model with flexible carcass

vertical load	F_z	4000	N
friction coefficient	μ	1.0	-
half contact length	a	0.0535	m
longitudinal carcass stiffness	c_x	5.50×10^5	N/m
lateral carcass stiffness	c_y	1.25×10^5	N/m
torsional carcass stiffness	c_ψ	4000	Nm/rad
tread element stiffness /m	c_p	10^7	N/m ²
composite tyre parameter	θ	4.77	-

Figure 9.10 presents the results for the two models. The range of the abscissa has been chosen such that precisely two wavelengths are covered and the distance rolled is large enough to have a situation close to the periodic state. Again, the agreement is quite good and we may have confidence in the model. The bottom diagram presents the variation of the slip angle. The top pair of diagrams shows the responses at the relatively long wavelength of 5m so that a condition closer to steady state has been reached. From Fig.9.7 it can be seen that at the maximum α of 0.16rad or almost 9° the aligning torque peak has been surpassed by far. This explains the two dips per wavelength. At a maximum of 0.08rad the peak has just been surpassed.

The less deep dips occurring in the upper curves of diagrams *b* and *d* are delayed with respect to the slip angle when this has reached its minimum value equal to zero. At steady state, when $\lambda \rightarrow \infty$, the moment (and the force) would

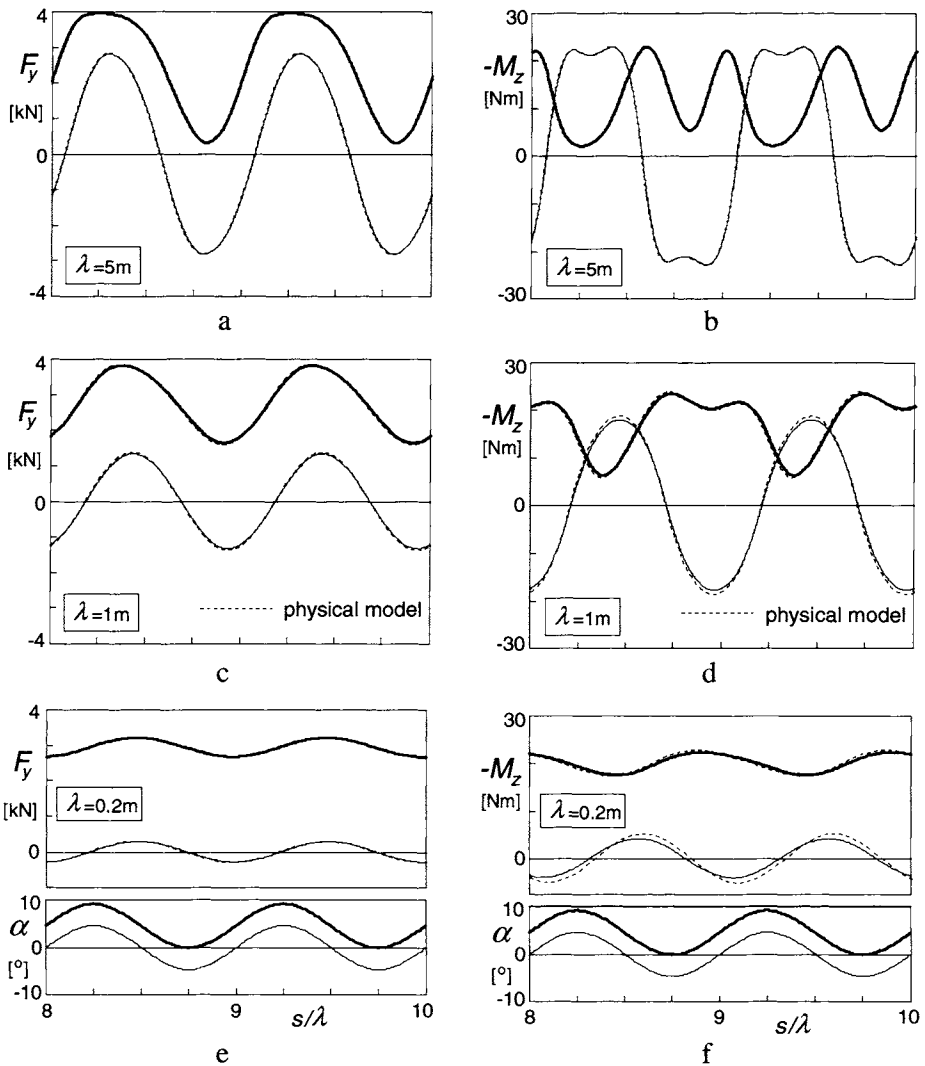


Fig. 9.10. Side force and aligning torque responses of the non-linear brush simulation model with flexible carcass to sinusoidal slip angle input of the wheel plane with a slip angle amplitude of 0.08rad and average levels of 0 (thin curves) and 0.08rad (fat curves), compared with results of the physical model (broken curves).

have become equal to zero at that instant. The deeper dips belong to the maxima of the slip angle variation. The considerable reduction in amplitude of the response at the shorter wavelengths nicely agrees with the findings of Fig.9.8. The force responses correspond almost perfectly with the outcome of the physical model. Evidently, a similar correspondence is expected to occur with the

response of the longitudinal force to longitudinal slip variations.

Turn Slip

The last item to be studied in the development of the contact model is the response to variations in path curvature while the slip angle remains zero. We will not attempt to develop a background analytical model but take a more heuristic route. The results will be checked by comparing these with the computed responses of the physical model. The responses derived for the string model with tread elements as presented in Chapter 5, especially the step responses to φ as depicted in Fig.5.21c and d (ex.tr.el.) and Fig.5.10 may be helpful. We observe that the force response is similar to that of the aligning torque to a step change in slip angle. In both cases the slope at the start is zero. The further approach of the force to its steady-state level is assumed to occur according to the first-order equation with σ_c as relaxation length. The zero slope at the start may be modelled by subtracting a response curve that starts with the same slope but dies out after having reached its peak. Such a short term response may be obtained by taking the difference of two responses each leading to the same level but starting at different slopes the difference of which should correspond to the initial slope of the uncorrected force response curve. For simplicity we take for one of the two responses the uncorrected force response, so that $\sigma_{F1} = \sigma_c$. The relaxation length of the second response should then be equal to $\sigma_{F2} = \sigma_c/2$. The resulting equations for the force response to the turn slip velocity $\dot{\psi}_c$ read:

$$\sigma_c \frac{d\varphi'_c}{dt} + |V_x| \varphi'_c = -\dot{\psi}_c \quad (9.56)$$

$$\sigma_{F2} \frac{d\varphi'_{F2}}{dt} + |V_x| \varphi'_{F2} = -\dot{\psi}_c \quad (9.57)$$

The transient turn slip for the force finally becomes:

$$\varphi'_F = \varphi'_c - (\varphi'_{F2} - \varphi'_{F1}) = 2\varphi'_c - \varphi'_{F2} \quad (9.58)$$

and the side force at pure path curvature is obtained from the non-linear steady-state response function:

$$F_y = F_y(\varphi'_F) \quad (9.59)$$

For the range of turn slip $a|\varphi| < 1/\theta$ the relation remains linear and equals:

$$F_y = C_{F\varphi 0} \varphi'_F = C_{Mac 0} \varphi'_F = \frac{2}{3} c_p a^3 \varphi'_F \quad (9.60)$$

The moment response may be divided into the response due to the contact patch length that involves lateral tread deflections, and the response due to tread width

giving rise to longitudinal deflections. First, we will address the moment generated by the brush model with zero width. Figures 5.9, 5.10 and 5.21 indicate that we are dealing here with a response that after having reached a peak tends to zero. Again we may model this behaviour by subtracting two first-order responses. For this, we introduce two transient turn slip quantities φ'_1 and φ'_2 with respective relaxation lengths: $\sigma_{\varphi 1}$ and $\sigma_{\varphi 2}$. The two differential equations become:

$$\sigma_{\varphi 1} \frac{d\varphi'_1}{dt} + |V_x| \varphi'_1 = -\dot{\psi}_c \quad (9.61)$$

$$\sigma_{\varphi 2} \frac{d\varphi'_2}{dt} + |V_x| \varphi'_2 = -\dot{\psi}_c \quad (9.62)$$

At zero speed the response of the difference would become:

$$\varphi'_1 - \varphi'_2 = -\left(\frac{1}{\sigma_{\varphi 1}} - \frac{1}{\sigma_{\varphi 2}} \right) \psi_c \quad (9.63)$$

The deflection angle of the tread due to transient spin is defined as:

$$\alpha_M = -2a(\varphi'_1 - \varphi'_2) \quad (9.64)$$

which at zero speed becomes:

$$\alpha_M = 2a \left(\frac{1}{\sigma_{\varphi 1}} - \frac{1}{\sigma_{\varphi 2}} \right) \psi_c \quad (9.65)$$

The condition to be satisfied is that the deflection angle is equal to the yaw angle. Hence, we have:

$$\frac{1}{\sigma_{\varphi 1}} - \frac{1}{\sigma_{\varphi 2}} = \frac{1}{2a} \quad (9.66)$$

In the case of small angles we may write for the moment:

$$M_z = -C_{Mac0} \alpha_M \quad (9.67)$$

From Eqs.(9.61,9.62) it can be assessed that the initial slope of the response of the moment to a step change in spin $\dot{\varphi}_c = -\dot{\psi}_c/V_x$ from zero to φ_{c0} turns out to be:

$$\frac{dM_z}{ds} = 2a C_{Mac0} \left(\frac{1}{\sigma_{\varphi 1}} - \frac{1}{\sigma_{\varphi 2}} \right) \varphi_{c0} = C_{Mac0} \varphi_{c0} \quad (9.68)$$

For the second condition to assess the ratios of the σ_{φ} 's to half the contact length a , the best fit of the remaining course of the step response may serve.

When the angle of rotation ψ continues to grow, the state of total sliding will be attained and the moment can be calculated to become:

$$M_{z\varphi\infty} = -\frac{3}{8}a\mu F_z \quad (9.69)$$

It has not been tried to derive the functional relationship between moment and increasing steer angle for the standing (non-rolling) brush model. The following non-linear function to describe the moment response in between the two extremes has been chosen:

$$M_z = -M_{z\varphi\infty} \sin \left\{ \arctan \left(\frac{C_{Mac0}}{M_{z\varphi\infty}} \varepsilon_\varphi \alpha_M \right) \right\} \quad (9.70)$$

The factor ε_φ has been introduced to have a parameter available to better approach the response shown by the physical model. The value 1.15 appeared to be appropriate. Similar to the relaxation length σ_c , Eqs.(9.29,24), the lengths $\sigma_{\varphi 1,2}$ are reduced in proportion with the magnitudes of transient turn slip quantities φ'_1 and φ'_2 .

For the evaluation of the model a comparison with the physical brush model has been executed. First, the flexible carcass is attached to the tread model, cf. Fig.9.5. To simulate this more complex situation, the approach of the enhanced transient model of Sec.7.3 has been adopted. The additional dynamic equations for the contact patch with mass m_c and moment of inertia I_c and carcass stiffnesses $c_{y,\psi}$ and damping coefficients $k_{y,\psi}$ read:

$$m_c (\dot{V}_{yc} + V_x \dot{\psi}_c) + k_y \dot{v} + c_y v = F_y \quad (9.71)$$

$$\dot{v} = V_{yc} - V_{sy} \quad (9.72)$$

$$I_c \ddot{\psi}_c + k_\psi \dot{\beta} + c_\psi \beta = M_z \quad (9.73)$$

$$\dot{\beta} = \dot{\psi}_c - \dot{\psi} \quad (9.74)$$

$$V_{syc} = V_{sy} + \dot{v} - V_x \beta \quad (9.75)$$

This extension of the model may, of course, also be used for the previously treated response to pure side slip. In fact, it is to be noted that the model for side slip, Eqs.(9.52-55), should be added to the spin model, Eqs.(9.61,9.62, 9.64,9.70), to correctly account for their interaction in the complete model with carcass compliance included. In the physical model the brush model automatically responds to both the side slip and spin. When the wheel plane is subjected to only side slip, the spin of the base line of the tread model remains very small and may be neglected. On the other hand, when the wheel is being steered with wheel side slip remaining zero (path curvature), the base line does show non-negligible side slip especially at shorter wavelengths where the moment

becomes considerable and as a result the base line is yawed and thus induces side slip. This effect vanishes at steady-state turning. However, if we would add the effect of tread width, the spin torque also acts at steady state and thereby contributes largely to the side force response to spin of the complete model.

Due to the complexity that arises when adding tread width to the brush model,

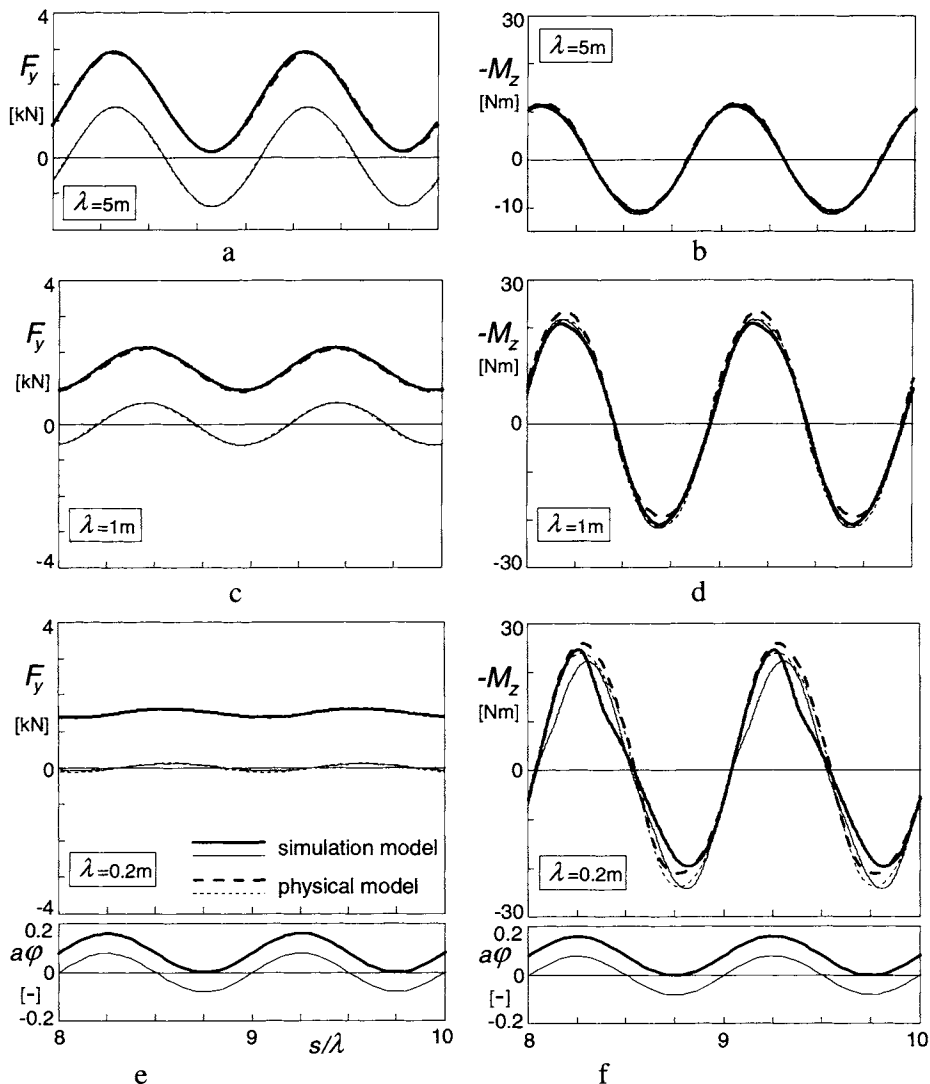


Fig. 9.11. Side force and aligning torque responses of the non-linear brush simulation model with flexible carcass to sinusoidal path curvature variations (turn slip at $\alpha = 0$) of the wheel with an amplitude of $a\phi$ equal to 0.08 and average levels of 0 (thin curves) and 0.08 (fat curves), compared with results of the physical model (broken curves).

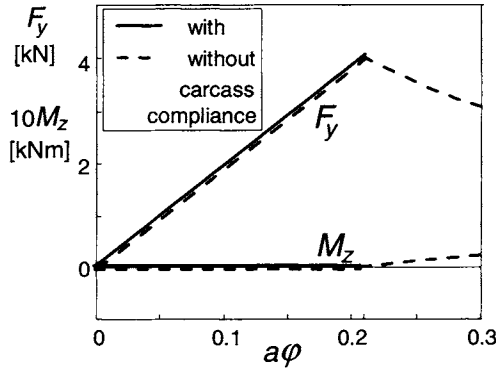


Fig. 9.12. Steady-state turn slip force and moment characteristics of the brush model both with and without flexible carcass. The effect of tread width has not been included.

cf. Chap.3, it has been decided to consider this aspect when dealing with the ultimate model adapted to the use of the *Magic Formula* in the next section.

The diagrams of Fig.9.11 present the computed responses to varying turn slip. It is seen that the correspondence with the physical model is quite good. The deformation of the moment response curve occurring at shorter wavelengths is caused by the extra moment ΔM_z generated through the base line slip angle variation.

As a reference, the steady-state characteristics of the force and moment response to turn slip, as computed for the single row brush model with and without carcass compliance have been shown in Fig.9.12. Up to $a\phi = 1/\theta$ the aligning torque remains zero which causes the characteristics for the cases without and with flexible carcass to become identical. The remaining course of the curves for the system including carcass compliance has not been computed as that part lies outside the range of evaluation.

Combined Slip

To cover the case of combined slip, also including longitudinal slip, the steady-state brush model characteristics are to be adapted as formulated in Chapter 3, Sec.3.2.3. In addition, the factor m that indicates the fraction of the contact length where adhesion occurs and is used to reduce the relaxation length σ_c is to be adapted by using the composite magnitude of slip of the contact patch:

$$\zeta'_c = \frac{\sqrt{\alpha_c'^2 + \kappa_c'^2}}{1 + \kappa_c'} \quad (9.76)$$

This expression holds because we have assumed that the brush model is isotropic. Using the magnitude of combined slip according to (9.76) the factor

m can be assessed :

$$m = 1 - \theta \zeta'_c \quad \text{if } \zeta'_c < 1/\theta \quad \text{else } m = 0 \quad (9.77)$$

Maurice (2000) found excellent agreement with the physical model for the combined slip cases: $\alpha_0 = 0.08\text{rad}$ and $\hat{\alpha} = 0.08\text{rad}$ and $\kappa_0 = 0.06$ and $\hat{\kappa} = 0.06$ with a phase difference of 45° and wavelengths of 0.2, 1 and 5m. For a more precise treatment with the interaction in the sliding range taken into account as well, we refer to the work of Berzeri et al. (1996).

Adding turn slip will influence the combined slip response further. The next section approaches this matter in a pragmatic way.

9.2.2. The Model Adapted to the Use of the *Magic Formula*

Now that we have treated all ingredients of the force and moment short wavelength responses to longitudinal, lateral and turn slip and have developed the structure of the contact model, we may carry on and show the performance of the model adapted to the use of the *Magic Formula* the parameters of which may have been assessed through full scale steady-state tyre measurements. The model includes the effect of tread width.

To illustrate the matter, we will here consider a simplified set of formulae for the steady-state responses, the complete version of which have been listed in Chapter 4, Secs.4.3.2 and 4.3.3. Only the case of combined side slip and turn slip will be considered. Adding braking or driving will not pose any problems.

A first problem that is encountered is the fact that in the model developed above where the contact patch is represented by the brush model, the steady-state characteristics employed belong to the brush model and not to the total model including the compliant carcass. In Fig.9.7 the calculated total model characteristics can be seen together with those of the contact patch alone.

An obvious solution is to model the contact patch characteristics with the *Magic Formulae*. These, however, will deviate from those assessed for the complete tyre because the contact patch 'sees' a slip angle that differs (is smaller) from that of the wheel plane. A set of adapted *MF* parameters may be established off-line for the contact patch or an iteration loop may be included to achieve the correct steady-state behaviour of the total model. A practical way has been found which employs a first-order feed-back loop with small time constant. Instead of introducing an additional first-order differential equation, the already present first-order equation for the transient side slip α' has been used. The diagram of Fig.9.13 illustrates the set-up. A similar approach is followed in Sec.9.3 to account for the camber angle of the belt being different from the

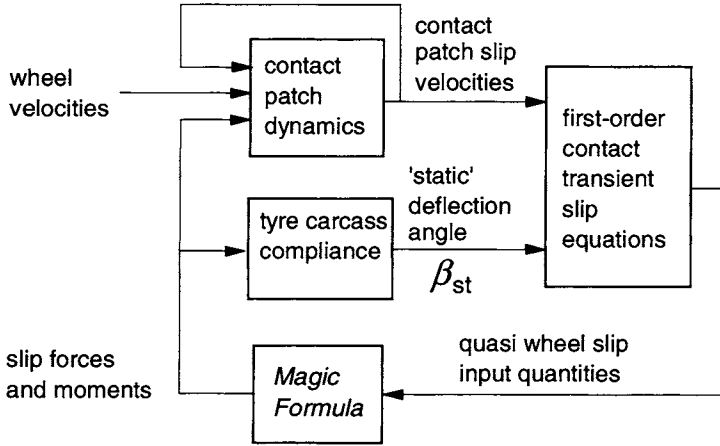


Fig. 9.13. Diagram explaining the model structure using the *Magic Formula*.

camber angle of the wheel plane.

The transient slip first-order differential equations listed below are identical to those derived in the previous section except for the first equation for the lateral transient slip. The factor \mathcal{E}_ϕ^* in (9.86) accounts for the effect of tread width.

transient slip equations for side slip, turn slip and camber

$$\sigma_c \frac{d\alpha'}{dt} + |V_x| \alpha' = -V_{\text{sync}} - |V_x| \beta_{\text{st}} \quad (9.78)$$

$$\sigma_2 \frac{d\alpha'_t}{dt} + |V_x| \alpha'_t = |V_x| \alpha' \quad (9.79)$$

$$\sigma_c \frac{d\varphi'_c}{dt} + |V_x| \varphi'_c = -\dot{\psi}_c \quad (9.80)$$

$$\sigma_{F2} \frac{d\varphi'_{F2}}{dt} + |V_x| \varphi'_{F2} = -\dot{\psi}_c \quad (9.81)$$

$$\sigma_{\varphi 1} \frac{d\varphi'_1}{dt} + |V_x| \varphi'_1 = -\dot{\psi}_c \quad (9.82)$$

$$\sigma_{\varphi 2} \frac{d\varphi'_2}{dt} + |V_x| \varphi'_2 = -\dot{\psi}_c \quad (9.83)$$

where in (9.78) the calculated deflection angle has been used:

$$\beta_{\text{st}} = M_z / c_\psi \quad (9.84)$$

composite transient slip quantities

$$\varphi'_F = 2\varphi'_c - \varphi'_{F2} \quad (9.85)$$

$$\varphi'_M = \varepsilon_\varphi^* \varphi'_c + \varepsilon_{\varphi 12} (\varphi'_1 - \varphi'_2) \quad (9.86)$$

dynamic contact patch equations

$$m_c (\dot{V}_{yc} + V_x \dot{\psi}_c) + k_y \dot{v} + c_y v = F_y \quad (9.87)$$

$$\dot{v} = V_{yc} - V_{sy} \quad (9.88)$$

$$I_c \ddot{\psi}_c + k_\psi \dot{\beta} + c_\psi \beta = M_z \quad (9.89)$$

$$\dot{\beta} = \dot{\psi}_c - \dot{\psi} \quad (9.90)$$

$$V_{syc} = V_{sy} + \dot{v} - V_x \beta \quad (9.91)$$

simplified side force and aligning torque Magic Formulae (MF)

$$F_y = D_y \sin\{C_y \arctan(B_y \alpha_y)\} \quad (9.92)$$

$$M_z = -tF_y + \Delta M_z + M_{zr} \quad (9.93)$$

$$C_y = P_{Cyl} \quad (9.94)$$

$$D_y = \mu F_z \cdot \zeta_2 \quad (9.95)$$

$$B_y = K_{y\alpha} / (C_y D_y) \quad (9.96)$$

$$K_{y\alpha} = C_{Fa0} \cdot \zeta_3 \quad (9.97)$$

$$\alpha_y = \alpha' + S_{Hy} \quad (9.98)$$

$$S_{Hy} = D_{Hy\varphi} \sin\{C_{Hy\varphi} \arctan(B_{Hy\varphi} R_o \varphi'_F)\} \quad (9.99)$$

$$t = D_t \cos\{C_t \arctan(B_t \alpha_t)\} \quad (9.100)$$

$$\alpha_t = \alpha'_t + S_{Ht} \quad (9.101)$$

$$S_{Ht} = 0 \quad (9.102)$$

$$D_t = q_{Dz1} R_o \cdot \zeta_5 \quad (9.103)$$

$$D_{r\varphi} = D_{Dr\varphi} \sin\{C_{Dr\varphi} \arctan(B_{Dr\varphi} R_o \varphi'_M)\} \quad (9.104)$$

$$M_{zr} = M_{z\varphi} \approx D_{r\varphi} \quad (9.105)$$

$$\Delta M_z = C_{\Delta M} (\alpha' - \alpha'_t) \quad (9.106)$$

$$\zeta_2 = \cos\{\arctan(B_{y\varphi} R_o \varphi'_F)\} \quad (9.107)$$

$$\zeta_3 = \cos\{\arctan(p_{Ky\varphi} R_o^2 \varphi'^2_F)\} \quad (9.108)$$

$$\zeta_5 = \cos\{\arctan(q_{Dt\varphi 1} R_o \varphi'_F)\} \quad (9.109)$$

factors reduced with slip

$$C_{\Delta M} = C_{Fa0} t_0 \cdot \max(1 - \theta \zeta', 0) \quad (9.110)$$

$$\sigma_c = a \cdot \max(1 - \theta \zeta', \varepsilon_{\lim}) \quad (9.111)$$

$$\sigma_2 = \frac{t_0}{a} \sigma_c \quad (9.112)$$

$$\sigma_{F2} = b_{F2} \sigma_c = 0.5 \sigma_c \quad (9.113)$$

$$\sigma_{\varphi 1} = b_{\varphi 1} \sigma_c \quad (9.114)$$

$$\sigma_{\varphi 2} = b_{\varphi 2} \sigma_c = \sigma_c / \left(\frac{1}{b_{\varphi 1}} - \frac{1}{2} \right) \quad (9.115)$$

with tyre composite parameter

$$\theta = \frac{C_{Fa0}}{3\mu F_z} \quad (9.116)$$

and the total magnitude of equivalent side slip

$$\zeta' = \frac{1}{1 + \kappa'} \sqrt{\left\{ |\alpha'| + a \varepsilon_{\varphi 12} |\varphi_1' - \varphi_2'| \right\}^2 + \left(\frac{C_{F\kappa 0}}{C_{Fa0}} \right)^2 \left\{ |\kappa'| + \frac{2}{3} b |\varphi_c'| \right\}^2} \quad (9.117)$$

where in the present application $\kappa' = 0$.

other parameter relations

$$C_{Fac0} = C_{F\kappa c0} \quad (9.118)$$

$$t_{c0} = q_{Dz1} R_o$$

$$C_{M\varphi^*c0} = (2/3)^2 b^2 C_{F\kappa c0}$$

$$C_{Mac0} = t_{c0} C_{Fac0}$$

$$C_{F\varphi c0} = C_{Mac0}$$

$$C_{M\varphi c0} = C_{M\varphi^*c0} - t_{c0} C_{F\varphi c0}$$

$$t_0 = t_{c0}$$

$$C_{Fa0} = C_{Fac0} / (1 + t_0 C_{Fac0} / c_\psi)$$

$$C_{Ma0} = t_0 C_{Fa0}$$

$$C_y = p_{Cy1}$$

$$B_t = q_{Bz1} C_{Fa0} / C_{Fac0}$$

$$C_t = q_{Cz1}$$

$$C_{F\varphi 0} = C_{F\varphi c0} + C_{Fac0} C_{M\varphi c0} / (c_\psi + C_{Mac0})$$

$$C_{M\varphi 0} = C_{M\varphi c0} c_\psi / (c_\psi + C_{Mac0})$$

$$B_{y\varphi} = p_{Dy\varphi 1} \quad (9.119)$$

$$C_{Hy\varphi} = p_{Hy\varphi 1}$$

$$D_{Hy\varphi} = p_{Hy\varphi 2}$$

$$B_{Hy\varphi} = C_{F\varphi 0} / (R_o C_{Hy\varphi} D_{Hy\varphi} C_{Fa0})$$

$$C_{Dr\varphi} = q_{Dr\varphi 1}$$

$$D_{Dr\varphi} = M_{z\varphi\infty} / \sin(0.5\pi C_{Dr\varphi})$$

$$K_{zR\varphi 0} = (C_{M\varphi 0} + t_0 C_{F\varphi 0}) / R_o$$

$$B_{Dr\varphi} = K_{zR\varphi 0} / (C_{Dr\varphi} D_{Dr\varphi})$$

$$M_{z\varphi\infty} = q_{Cr\varphi 1} R_o \mu F_z$$

$$k_{\text{ycrit}} = 2\sqrt{(m_c c_y)} \quad (9.120)$$

$$k_{\psi\text{crit}} = 2\sqrt{(I_c c_\psi)}$$

$$k_y = \zeta_k k_{\text{ycrit}}$$

$$k_\psi = \zeta_k k_{\psi\text{crit}}$$

Table 9.2. Parameter values for tyre model with *Magic Formula* including quantities introduced later on

F_z	4000N	μ	1.0	p_{Cy1}	1.2	$p_{Ky\phi1}$	1.0
c_y	125×10^3 N/m	C_{Fkc0}	$15F_z$	q_{Bz1}	22	$p_{Hy\phi1}$	0.15
c_ψ	4×10^3 Nm/rad	a	0.0535 m	q_{Cz1}	1.192	$p_{Hy\phi2}$	1.0
m_c	0.5 kg	b	$0.9a$	q_{Dz1}	0.05	$q_{Cr\phi1}$	0.12
I_c	0.0005 kgm ²	R_o	0.3 m	$p_{Dy\phi1}$	0.4	$q_{Dr\phi1}$	1.0
ζ_k	0.1	ε_ϕ^*	1.0	$\varepsilon_{\phi12}$	4.0	$q_{Dt\phi1}$	10
b_{F2}	0.5	$b_{\phi1}$	0.5	$b_{\phi2}$	1/1.5		
ε_{lim}	0.1	V_{low}	1 m/s	m_{qc}	400 kg	c_o	2.0

Steady-State, Step Response and Frequency Response Characteristics

To demonstrate the performance of the model, a number of typical characteristics will be presented. The hypothetical steady-state pure side slip and pure turn slip characteristics of the model have been given in Fig.9.14.

The step response graphs of Fig.9.15 show the proper shapes of the various curves, notably the initial horizontal tangent of the response curves of the side force to turn slip and of the moment to side slip, also shown in Fig.5.21 (no tread width). Also, the peak of the moment response curve to spin and the dip of the

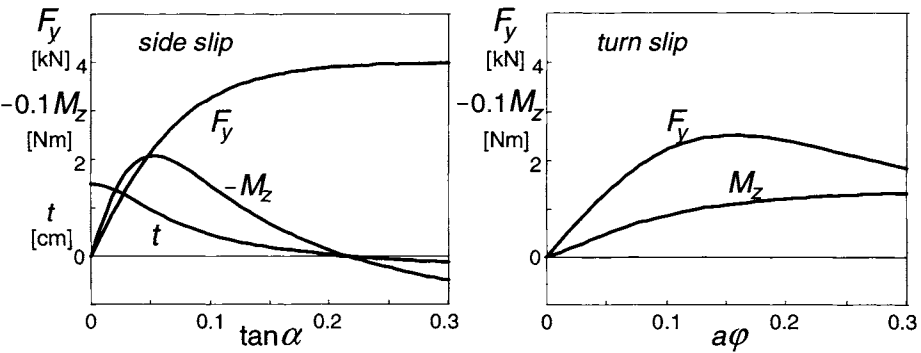


Fig. 9.14. Steady-state side slip and turn slip force and moment characteristics of the overall tyre model as defined by the *Magic Formula*. The effect of tread width has been included.

curve of the moment response to steer angle are exhibited as expected.

Figure 9.16 presents the frequency response functions of the linearised system at zero average side and turn slip with tread width effect included. The curves may be compared with those of the string model with tread elements, cf. Fig.5.23 (with zero tread width). In Fig.9.17 the Nyquist plots of the moment response to steer angle have been depicted. The upper diagram shows the influence of tread width by changing the parameter ε_φ^* . If equal to zero the thin tyre is represented. The value 1 corresponds with the baseline configuration. The lower graph provides insight in the influence of the parameter $\varepsilon_{\varphi 12}$ that governs the magnitude of the effect of the transient yaw deflection angle α_M (9.64,9.86). The value 4 is used in the baseline configuration. When compared with the plots of Figs.5.27 and 5.35 it may be concluded that the model is capable of approaching the responses of more complex infinite order models and of actual tyres.

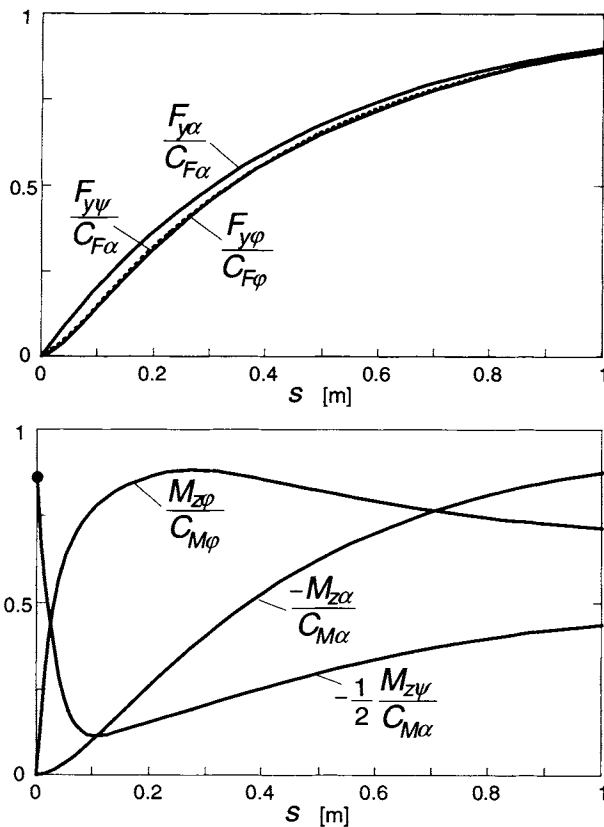


Fig. 9.15. Step response curves of the side force and of the aligning torque to side slip α , turn slip (path curvature) φ and steer angle ψ .

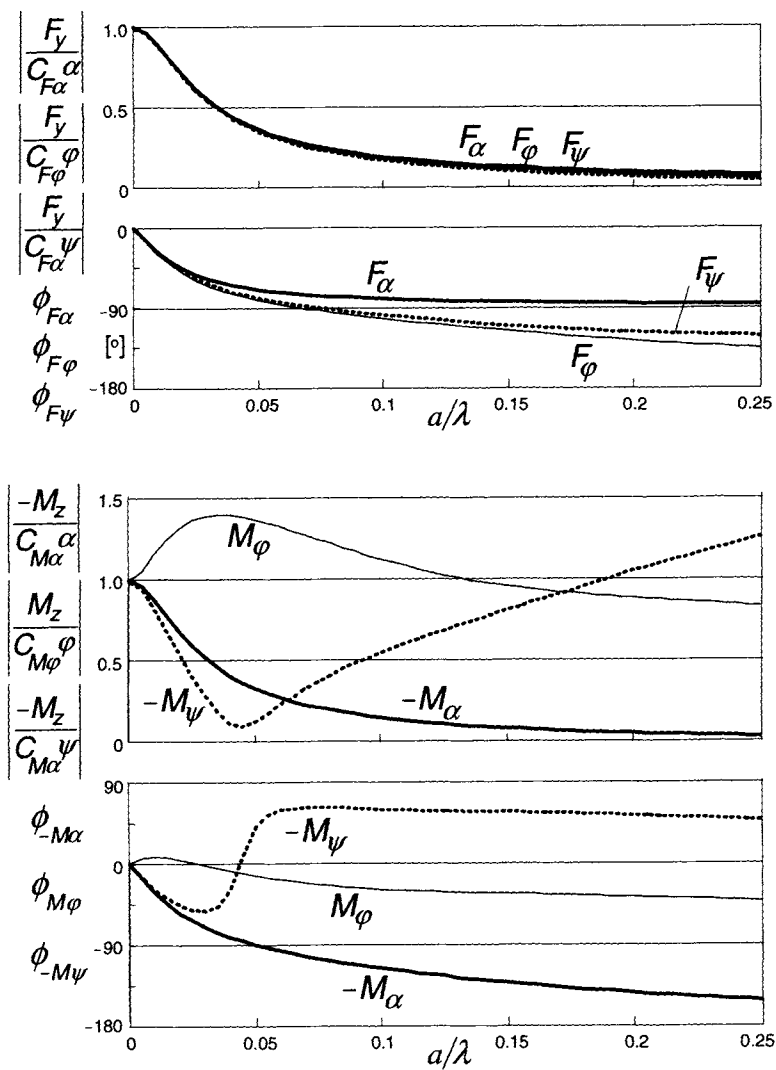


Fig. 9.16. Frequency response function of system with tread width. Curves for the force and moment responses to side slip α , turn slip (path curvature) ϕ and steer angle ψ have been indicated.

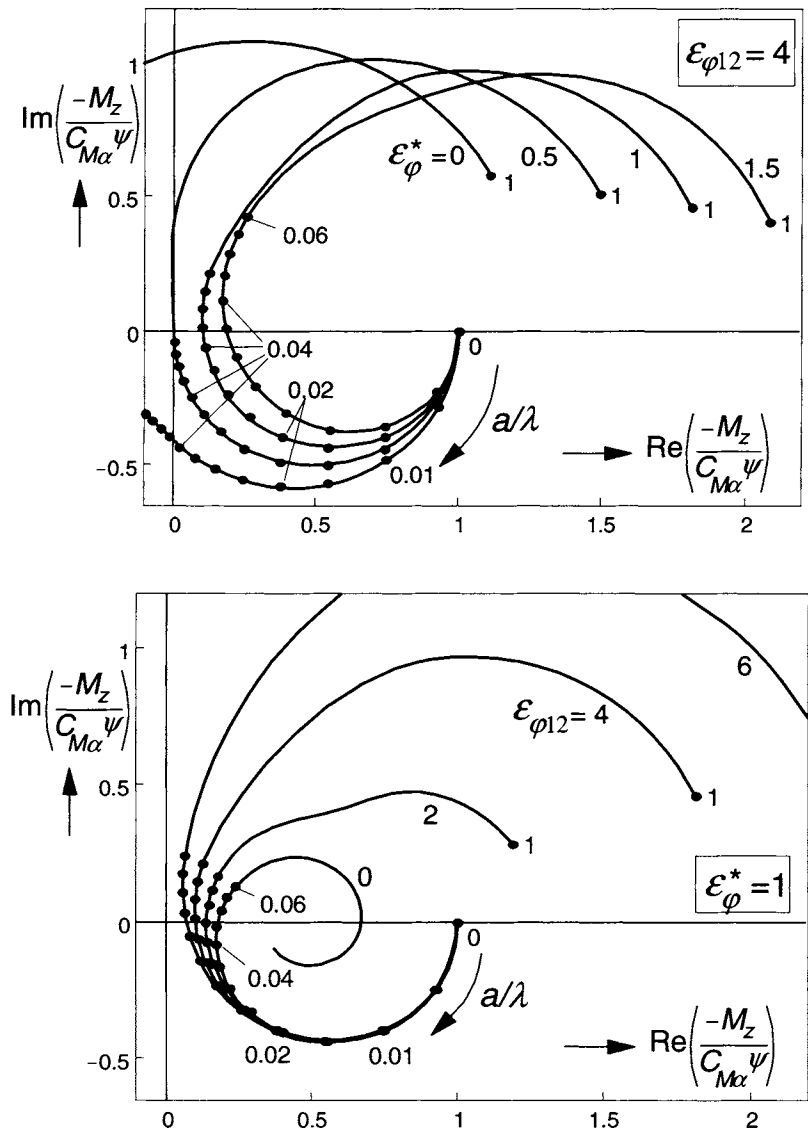


Fig. 9.17. Nyquist frequency response plots of the aligning torque to steer angle. Upper diagram: influence of tread width (4 is baseline value), lower diagram: influence of the transient yaw deflection response to turn slip (4 is baseline value).

Large Slip Angle and Turn Slip Response Simulations

The same sinusoidal manoeuvres have been simulated as was done before with the brush based contact model. The complete non-linear set of equations (9.78) to (9.120) have been used with parameters listed in Table 9.2.

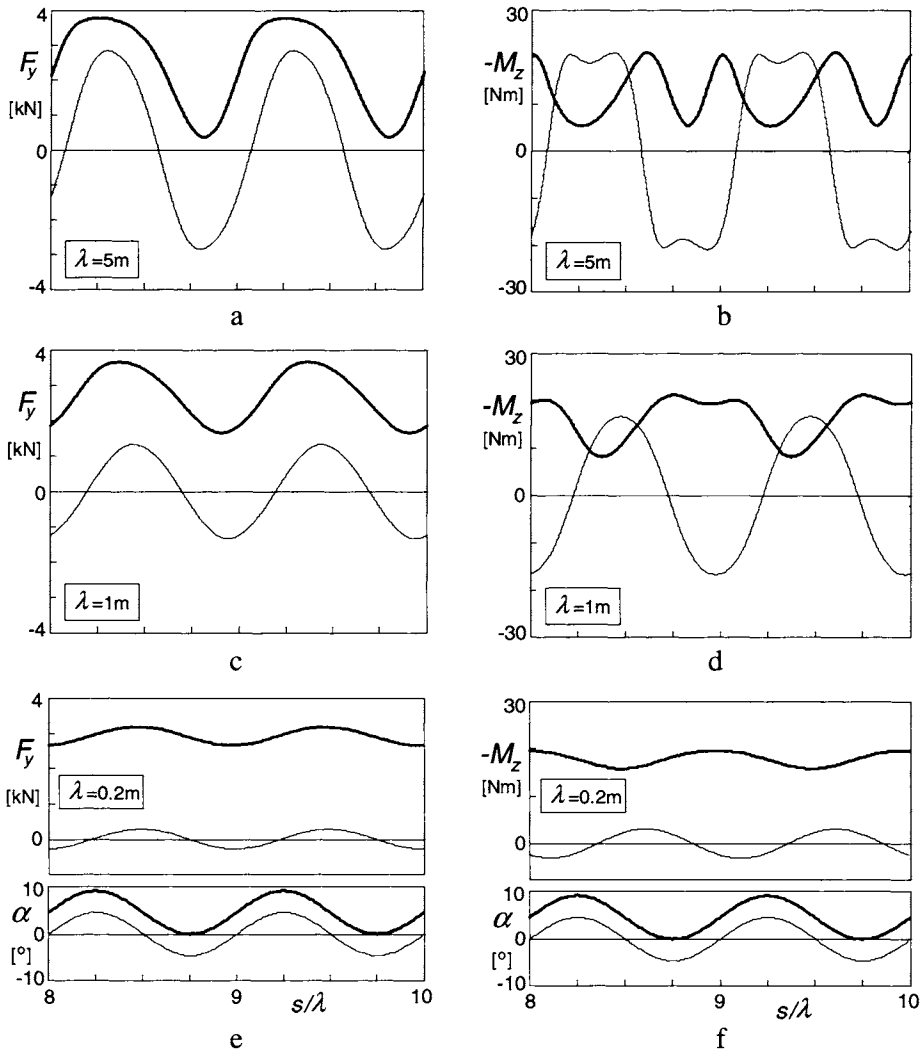


Fig. 9.18. Side force and aligning torque responses of the *Magic Formula* based simulation model with flexible carcass and finite tread width to sinusoidal slip angle input of the wheel plane with a slip angle amplitude of 0.08rad and average levels of 0 (thin curves) and 0.08rad (fat curves).

The slip angle variation is sinusoidal around average levels $\alpha_0 = 0$ and 0.08rad with one amplitude: $\hat{\alpha} = 0.08\text{rad}$ at three wavelengths: $\lambda = 0.2, 1$ and 5m . Similarly, the turn slip has two average levels: $a\varphi_0 = 0$ and 0.08 and one amplitude: $a\hat{\varphi} = 0.08$, also at wavelengths: $\lambda = 0.2, 1$ and 5m .

The diagrams of Figs.9.18-19 present the results. We observe that the curves

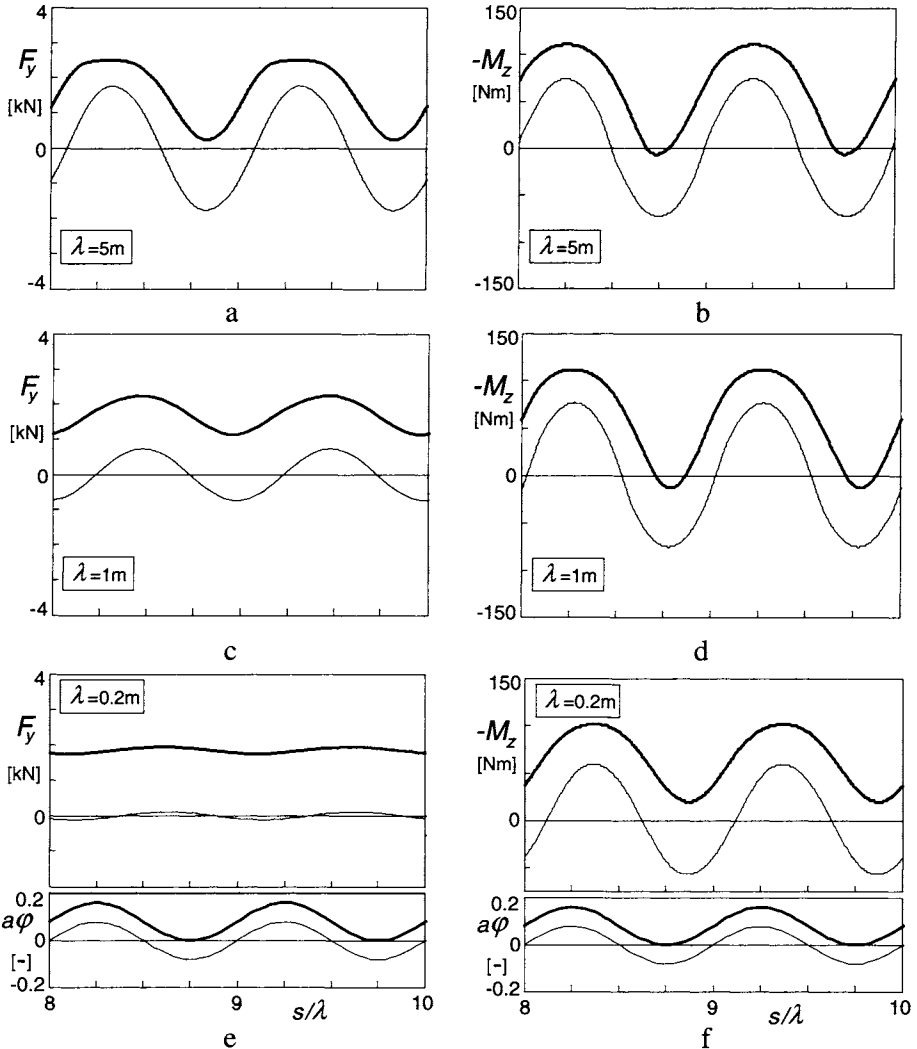


Fig. 9.19. Side force and aligning torque responses of the *Magic Formula* based simulation model with flexible carcass and finite tread width to sinusoidal path curvature variations (turn slip at $\alpha = 0$) of the wheel plane with an amplitude of $a\varphi$ of 0.08 and average levels of 0 (thin curves) and 0.08 (fat curves).

are quite similar to those depicted in the Figs.9.10 and 9.11. Only, as expected, the moment response to turn slip is very much affected by the now introduced effect of the tyre tread width.

Maurice has conducted extensive experiments with a 205/60R15 91V tyre at 2.2 bar inflation pressure on a 2.5m drum test rig. The diagrams of Fig.9.20a present the computed results compared with experimental data for the case of pure side slip. The experiments have been carried out at very low speed to avoid inertia effects of the moving tyre. The wavelength ranges from 0.3 to 2.4m. The upper diagram refers to the case of zero average slip angle and 4° amplitude. The lower diagram shows the responses around an average slip angle of 4° which causes the curves to deviate considerably from the input sinusoidal shape. The curves clearly show that a shorter wavelength causes the response amplitude to

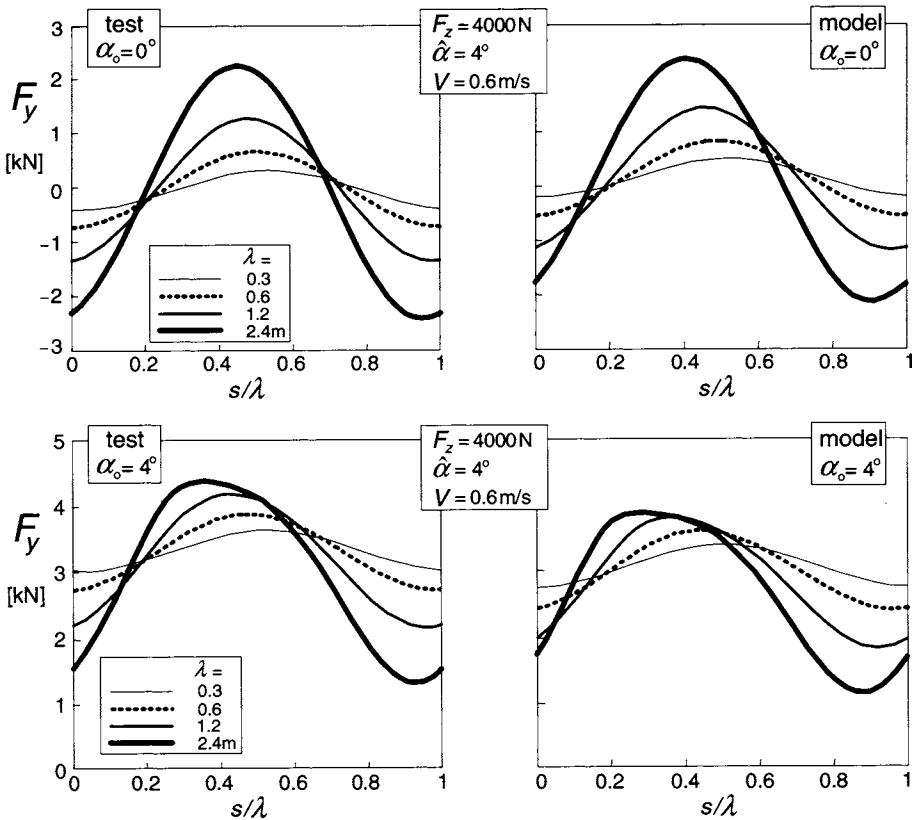
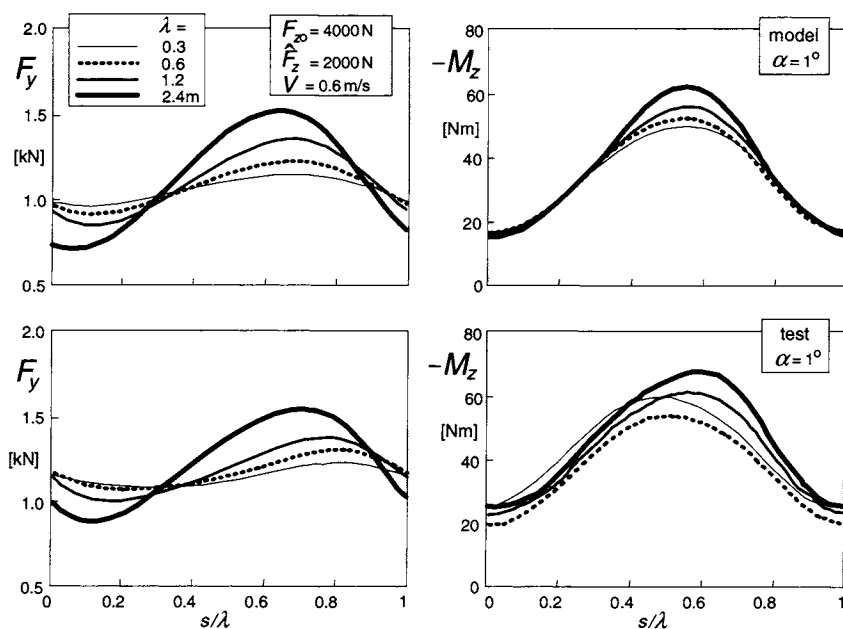


Fig. 9.20a. Comparison of theoretical model calculations and experimental results performed at 0.6 m/s on a 2.5 m drum (Maurice). The curves cover one wavelength of the periodic responses to sinusoidal slip angle variations. Force response to slip angle variations at two levels of side slip.



decrease and the phase lag to increase. It can also be observed that the responses

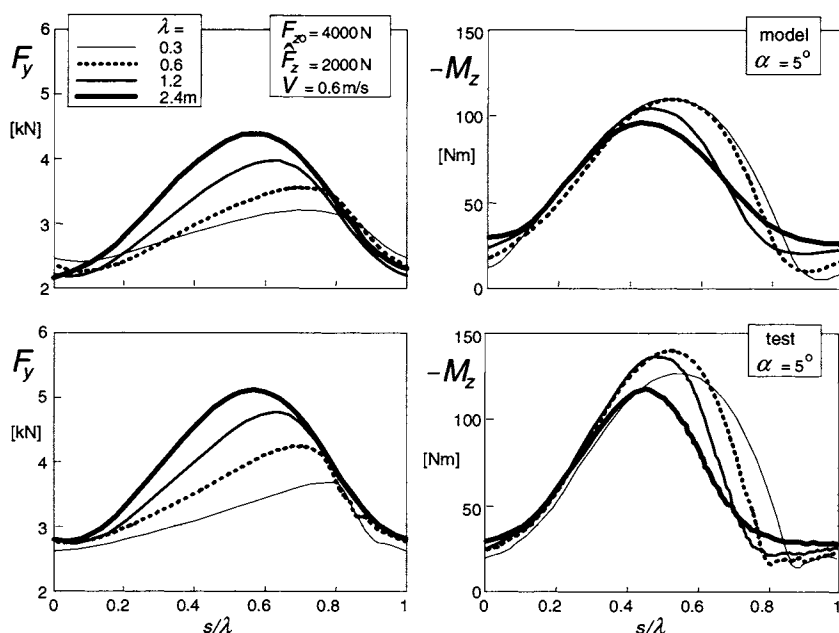


Fig. 9.20b. Comparison of theoretical model calculations and experimental results performed at 0.6 m/s on a 2.5 m drum (Maurice). The curves cover one wavelength of the periodic responses to sinusoidal load variations. Force and moment response to vertical load variations at two values of slip angle.

occur more quickly at larger levels of slip which is due to the with slip sharply decreasing relaxation length. The magic formula was used to model the steady-state characteristics. The parameters were obtained from separate tests performed on the drum at the much higher speed of 60 km/h. The different conditions may explain the deviation in level of the calculated with respect to the measured responses.

Figure 9.20b present the comparison with the results of a second series of experiments at same conditions. Here, the vertical load is changed sinusoidally while the slip angle is kept at a low level and at a higher level. The results are similar to those discussed in Chapter 8, Fig.8.9. The moment response seems to be improved with the more complex tyre model.

The agreement of the computed results with experimental data is quite good. As has been reported by Maurice, also for the moment response a rather good agreement has been established. Since at the maximum slip angle of 8° the peak of the moment characteristic has been surpassed, the result becomes quite sensitive to small differences between actual and model steady-state characteristics of the aligning torque.

9.2.3. Parking Manoeuvres

Parking manoeuvres take place at very low or zero speed. The torque acting on the tyre at such conditions may become very large. The influence of the finite tread width is essential as the response to spin is now predominant. We might employ the equations developed above but then we should take care of the integration of the spin velocity to properly limit the built-up of the yaw transient slip. Similar problems arose when considering the problem of braking to stand-still or starting from stand-still, cf. Sec.8.6, Eqs.(8.112,8.113).

To achieve a much better agreement with experimental evidence, a different approach will be followed in the present application. It may be noted that an important characteristic is actually still missing. For the brush based model Eq.(9.70) was used. The equation governs the variation of the aligning torque M_z that arises when the non-rolling tyre is steered and the steer angle ψ is increased from zero to and beyond the state of full sliding. Ultimately, the torque reaches the magnitude that would also arise when the rolling tyre is subjected to a constant rate of turning $d\psi/dt$ (while the slip angle remains zero), at a forward speed V_x that decreases to zero. Then, the radius of turn R reduces to zero and thus the spin approaches infinity. Figure 9.21 illustrates the situation.

The missing characteristic will be modelled by using a for this purpose

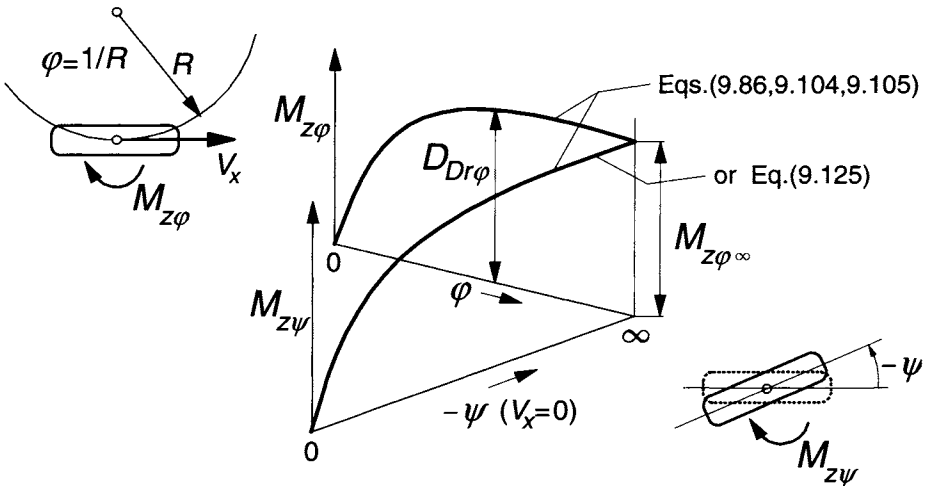


Fig. 9.21. Approaching the maximum torque at stand-still in two ways: 1. by decreasing the turn radius R to zero, 2. by increasing the steer angle $-\psi$ while standing still.

adequate model that has been developed by Van der Jagt (2000). In his dissertation a model study was discussed that is especially aimed at the generation of a proper moment response to steering at very low or zero speed. First, the brush model was used to gain general insight into the phenomena that occur. Qualitatively good results have been obtained using this model, notably when a sinusoidal steer angle variation is imposed and the state of almost full sliding is attained periodically. For practical usage, a special type of model was developed of a nature completely different from the models used so far. Since this model appears to perform very well in the near zero speed range we have tried to incorporate Van der Jagt's model in the existing model structure. For a gradual transition from the new type of model to the existing one when the speed approaches and surpasses a low speed threshold has been taken care of.

The principle of Van der Jagt's approach is that at a given rate of change of the steer input the growth rate of the tyre angular deflection β decreases in proportion with a function of the remaining difference between the maximum achievable deflection and the current deflection. The torsional stiffness is assumed to be a constant and the resulting characteristic of the torque becomes similar to a first-order response function. The calculated moment gradually approaches its maximum value. When the direction of rotation of the wheel about the vertical axis is changed, the distance to the new, opposite, peak torque is large and, accordingly, the rate of reduction of the moment is large as well. It is this feature of the model that is attractive since a similar behaviour has been found to occur with the actual tyre subjected to an alternating left and right

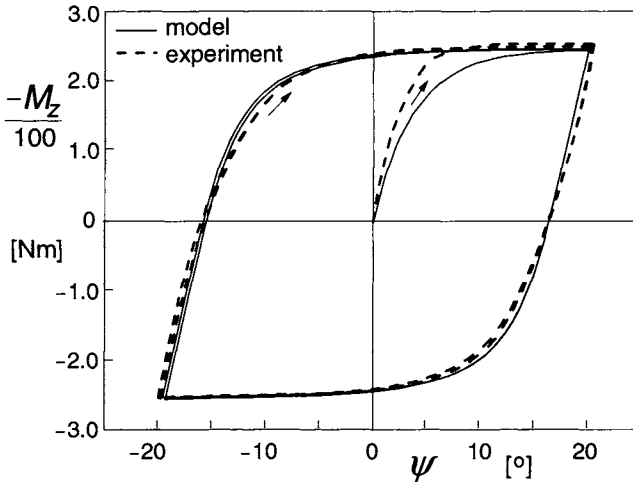


Fig. 9.22. Calculated and experimentally assessed variation of the moment vs steer angle for a non-rolling tyre pressed against a flat plate at a load $F_z = 4800\text{N}$.

sequence of turning. The equations that govern the moment generation at stand-still are as follows:

$$\dot{\beta} = - \left(1 - p \left| \frac{M_{z\psi}}{M_{z\varphi_\infty}} \right|^{c_o} \right) \dot{\psi} \quad (9.121a)$$

$$M_{z\psi} = C_{M\psi} \beta \quad (9.121b)$$

$$p = 0 \quad \text{if} \quad \text{sgn}\beta \neq -\text{sgn}\dot{\psi} \quad \text{else} \quad p = 1 \quad (9.121c)$$

For the parameter value $c_o = 2$, Fig.9.22 presents the calculated variation of the torque vs the steer angle compared with experimentally obtained results as reported by Van der Jagt. The non-rolling tyre (size P205/65R15) is loaded to 4800N on a flat plate and subsequently steered at a rate of + and - 1 deg./s. The correspondence is quite good perhaps except for the initial phase where the wheel starts to be steered from the condition where $M_z = 0$. To improve the model performance Van der Jagt suggests to use an exponent c_o the value of which depends on the last extreme of the deflection angle β . For possible further refinements of the model we refer to the original work.

When, instead of the new approach, the *Magic Formula* would be used with the integration limitation as suggested according to Eqs.(8.112,8.113), a sharp peak would arise in the curve where the direction of turning is changed. As a result, the moment decreases at a much slower rate than shown by the test result.

The problem is now how to integrate the new model feature in the original model structure. The transient slip quantity $\varphi'_{M'}$ Eq.(9.86), may be recognised

to be proportional with the deflection angle. As can be seen from Eqs. (9.80,9.82,9.83,9.86) this quantity is obtained through integration of:

$$\dot{\varphi}'_M = \varepsilon_{\varphi}^* \dot{\varphi}'_c + \varepsilon_{\varphi 12} (\dot{\varphi}'_1 - \dot{\varphi}'_2) \quad (9.122)$$

In the new configuration, the integration is conducted at a gradually decreasing rate while approaching the maximum torque value. We have:

$$\dot{\varphi}'_M = \left(1 - w_{Vlow} p \left| \frac{M_{z\varphi}}{M_{z\varphi\infty}} \right|^2 \right) \dot{\varphi}'_M \quad (9.123)$$

$$\text{where } p = 0 \quad \text{if} \quad \text{sgn } \dot{\varphi}'_M \neq \text{sgn } \dot{\varphi}'_M \quad \text{else} \quad p = 1. \quad (9.124)$$

At zero speed $w_{Vlow} = 1$. The moment is found with the linear function, cf. (9.104):

$$M_{z\varphi} = D_{Dr\varphi} C_{Dr\varphi} B_{Dr\varphi} R_o \varphi'_M \quad (9.125)$$

For the standing tyre with speed V_x equal to zero the response to alternating steer angle variations will follow a course similar to that of Fig.9.22.

It is now desired to gradually change to the original equations when the tyre starts rolling. The transition is accomplished by adding up the following two components. The first one decreases in magnitude with increasing speed until it vanishes at $V_x = V_{low}$ while the second part increases from zero to its full value also at $V_x = V_{low}$. For the gradual change, the following speed window is used:

$$w_{Vlow} = \frac{1}{2} \left\{ 1 + \cos \left(\pi \frac{V_x}{V_{low}} \right) \right\} \quad \text{if } |V_x| < V_{low} \quad \text{else } w_{Vlow} = 0 \quad (9.126)$$

With this quantity (already used in (9.123)) the first part that prevails at low speed becomes:

$$M_{z\varphi 1} = w_{Vlow} \cdot D_{Dr\varphi} C_{Dr\varphi} B_{Dr\varphi} R_o \varphi'_M \quad (9.127a)$$

and the fraction obtained from the original (here simplified) Eqs.(9.105,9.104):

$$M_{z\varphi 2} = (1 - w_{Vlow}) \cdot D_{Dr\varphi} \sin \left\{ C_{Dr\varphi} \arctan(B_{Dr\varphi} R_o \varphi'_M) \right\} \quad (9.127b)$$

The resulting expression for the spin moment now reads:

$$M_{z\varphi} = M_{z\varphi 1} + M_{z\varphi 2} \quad (9.128)$$

A similar method may be employed to improve the low speed model for the side force responding to lateral motions of the contact patch (cf. Fig.9.29, point S) and for the fore and aft force to longitudinal motions of the same point S.

The adapted model will now be applied to the simulation of the motion of a rigid quarter car model with mass m_{qc} that, while a sinusoidal steering input is applied, starts moving after 1.6sec. with a linearly increasing speed. The lateral

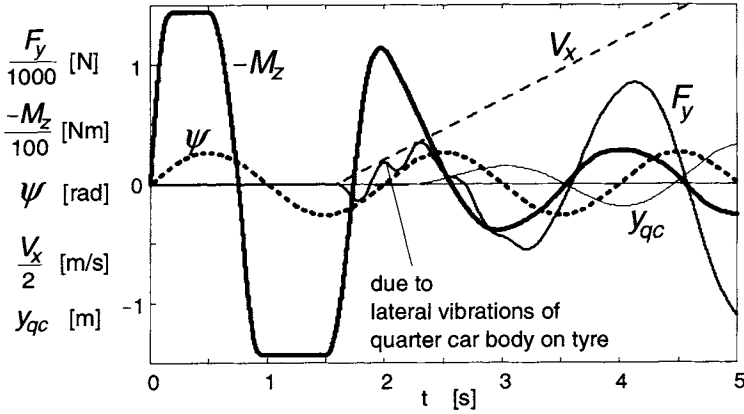


Fig. 9.23. Simulation results of a parking manoeuvre (car leaving the parking lot while steering sinusoidally).

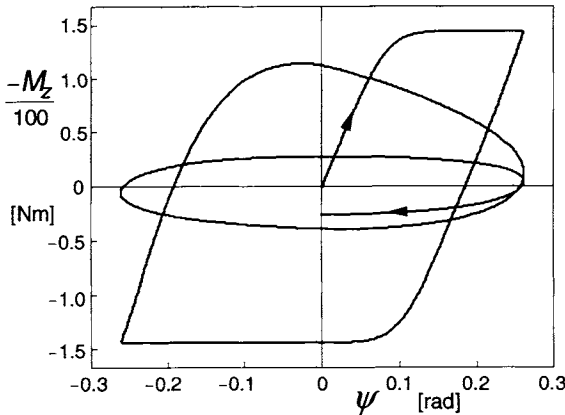


Fig. 9.24. The steer torque plotted vs steer angle during the manoeuvre of Fig.9.23.

acceleration of the quarter car axle results from the action of the side force that begins to develop after the wheel has started to roll:

$$\ddot{y}_{qc} = \frac{F_y}{m_{qc}} \quad (9.129)$$

The lateral wheel slip velocity is now not only a result of the yaw angle at a forward speed of the vehicle \dot{x}_{qc} but also due to the lateral velocity of the wheel axle \dot{y}_{qc} . We have:

$$V_{sy} = -\dot{x}_{qc} \sin \psi + \dot{y}_{qc} \cos \psi \quad (9.130)$$

which serves as an input into the equations (9.88,9.91). The additional parameter values have been appended in Table 9.2.

Figure 9.23 shows the courses of variation of various quantities vs time. Simultaneously, in Fig.9.24, the moment is plotted vs steer angle. Several phenomena occur that deserves to be noted. The steer angle has an amplitude that is large enough to attain a level of the moment close to its maximum. The moment starts to decrease in magnitude as soon as the steer angle passes its peak value. The moment changes sign before the steer angle does the same. After 1.6 seconds the forward speed increases linearly with time and the side force starts to built up as a result of the slip angle that begins to develop. The car shows a lateral vibration in the low speed range as indicated by the fluctuations of the side force. Evidently, the quarter car vibrates against the lateral tyre stiffness. The moment amplitude decreases as the spin diminishes in amplitude due to the increasing speed. The side force amplitude increases because of the larger lateral oscillations of the quarter car mass induced by the increasing speed of travel at the constant steer input pattern with time. The loops shown in Fig.9.24 give a nice impression of the transition from the situation at stand-still to the condition at higher speeds. At stand-still the moment varies in accordance with the diagram of Fig.9.22.

As mentioned before, to get a more accurate calculation of responses to lateral and circumferential wheel displacements at or near forward speed equal to zero, one might apply, instead of the abrupt integration limitation suggested earlier, Eqs.(8.112) and (8.113), the same structure of additional equations (9.123) and (9.124) and an adaptation such as achieved in Eq.(9.128).

9.3. Tyre Dynamics

The contact patch model has been used above in connection with a flexible carcass. In the present section the inertia of the belt will be introduced. Since we restrict the application of the model to frequencies lower than ca. 60Hz the belt may be approximated as a rigid ring that is attached to the wheel rim through flexible side walls. To ensure that the total static tyre stiffness remains unchanged, residual springs have been introduced between contact patch and belt. In certain cases, a by-pass spring directly connecting rim and contact patch may be needed to improve model accuracy.

9.3.1. Dynamic Equations

As depicted in Fig.9.25, the wheel axle position is defined by the location of

Their components are defined with respect to the (A, ξ, η, ζ) triad. The first of the two sets of first-order differential equations for the six degrees of freedom reads:

dynamic belt equations

$$m_b(\dot{V}_{b\xi} - V_{b\eta}\omega_{b\zeta}) + k_{bx}\dot{x}_b^r + c_{bx}x_b^r + k_{bz}\Omega z_b^r = K_{c\xi} \quad (9.131)$$

$$m_b\dot{V}_{b\zeta} + k_{bz}\dot{z}_b^r + c_{bz}z_b^r - k_{bx}\Omega x_b^r = K_{c\zeta} \quad (9.132)$$

$$I_{by}\dot{\omega}_{b\eta} + k_{b\theta}\dot{\theta}_b^r + c_{b\theta}\theta_b^r = T_{c\eta} \quad (9.133)$$

$$m_b(\dot{V}_{b\eta} + V_{b\xi}\omega_{b\zeta}) + k_{by}\dot{y}_b^r + c_{by}y_b^r = K_{c\eta} \quad (9.134)$$

$$I_{bx}\dot{\omega}_{b\xi} + I_{by}\Omega\omega_{b\zeta} + k_{b\gamma}\dot{\gamma}_b^r + c_{b\gamma}\gamma_b^r + k_{b\psi}\Omega\psi_b^r = T_{c\xi} \quad (9.135)$$

$$I_{bz}\dot{\omega}_{b\zeta} - I_{by}\Omega\omega_{b\xi} + k_{b\psi}\dot{\psi}_b^r + c_{b\psi}\psi_b^r - k_{b\gamma}\Omega\gamma_b^r = T_{c\zeta} \quad (9.136)$$

Several coupling terms show up. These are due to the gyroscopic effect and due to the action of the rotating radial dampers with resulting coefficient $k_{bx} = k_{bz}$ and the lateral dampers with resulting angular damping coefficients $k_{b\psi} = k_{b\gamma}$. Figure 9.26 illustrates the mechanism that gives rise to the interaction terms. The example concerns the term $k_{bz}\Omega z_b^r$ in (9.131). The following relations between the two sets of wheel and axle angular velocities hold:

$$\omega_\xi = \dot{\gamma} \quad (9.137)$$

$$\omega_\eta = -\Omega + \dot{\psi} \sin\gamma \approx -\Omega + \dot{\psi} \gamma \quad (9.138)$$

$$\omega_\zeta = \dot{\psi} \cos\gamma \approx \dot{\psi} \quad (9.139)$$

For the relative displacements between belt and wheel rim we have the second set of six first-order differential equations:

$$\dot{x}_b^r = V_{b\xi} - V_\xi \quad (9.140)$$

$$\dot{y}_b^r = V_{b\eta} - V_\eta \quad (9.141)$$

$$\dot{z}_b^r = V_{b\zeta} - V_\zeta \quad (9.142)$$

and

$$\dot{\gamma}_b^r = \omega_{b\xi} - \dot{\gamma} \quad (9.143)$$

$$\dot{\theta}_b^r = \omega_{b\eta} + \Omega - \dot{\psi}(\gamma + \gamma_b^r) \quad (9.144)$$

$$\dot{\psi}_b^r = \omega_{b\zeta} - \dot{\psi} \quad (9.145)$$

The forces and moments appearing in the right-hand members of Eqs.(9.131-

136) can be expressed in terms of the forces acting in the residual springs that connect the contact patch with the belt. The residual spring deflections as defined in the model can be observed in greater detail in Fig.9.27. The directions of the residual spring forces and moments are defined to act parallel to the moving axes system (C,x,y,z) with the z axis normal to the road plane. Also, the vertical forces F_z are defined here, in contrast to the definition adopted in the remainder of this book, according to the consistent SAE convention. For the normal wheel load acting from road to tyre we introduce the positive quantity F_N . We have in case of a horizontal road plane with products of angles neglected and r_l denoting the loaded radius:

$$K_{c\xi} = F_{cx} \quad (9.146)$$

$$K_{c\zeta} = F_{cz} - \gamma F_{cy} \quad (9.147)$$

$$T_{c\eta} = r_l F_{cx} + M_{cy} \quad (9.148)$$

$$K_{c\eta} = F_{cy} + \gamma F_{cz} \quad (9.149)$$

$$T_{c\xi} = -r_l F_{cy} - (r_l \gamma_b - y_c^r) F_{cz} + M_{cx} \quad (9.150)$$

$$T_{c\zeta} = M_{cz} - y_c^r F_{cx} \quad (9.151)$$

Obviously, a proper axes transformation is to be performed if the road plane is not horizontal. As a result, transverse and forward slopes will affect the terms appearing in the right-hand members of Eqs.(9.146-151). It is left to the user to introduce these transformations.

The contact patch body is subjected to forces acting in the residual springs (subscript c) and external forces acting from road surface to contact patch

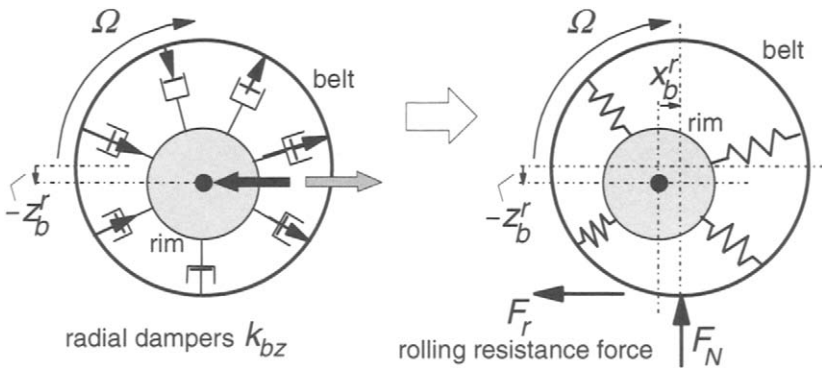


Fig. 9.26. The rotating radial dampers of the vertically deflected tyre gives rise to a resulting fore and aft force acting between belt and rim. The resulting longitudinal deflection produces a rolling resistance force F_r through the action of the normal load F_N .

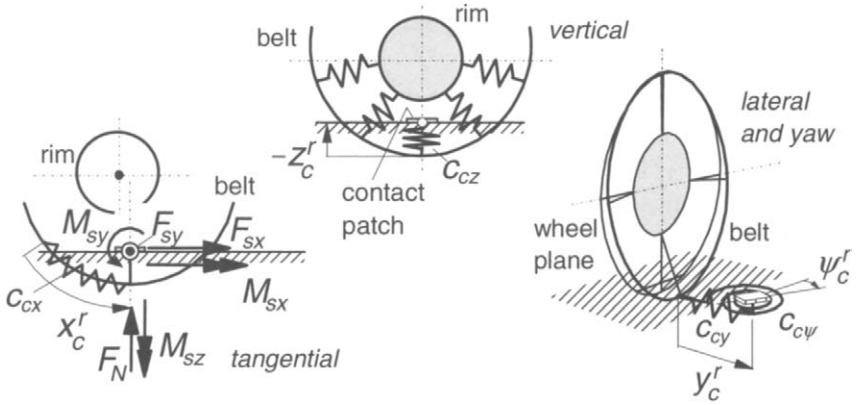


Fig. 9.27. Deflections of the residual springs attaching contact patch to belt.

(subscript $_s$). Figure 9.28 illustrates the situation. The differential equations that govern the horizontal dynamics of the contact patch body read:

dynamic contact patch equations

$$m_c(\dot{V}_{cx} - V_{cy}\dot{\psi}_c^r) + k_{cx}\dot{x}_c^r + c_{cx}x_c^r = F_{sx} \quad (9.152)$$

$$m_c(\dot{V}_{cy} + V_{cx}\dot{\psi}_c^r) + k_{cy}\dot{y}_c^r + c_{cy}y_c^r = F_{sy} \quad (9.153)$$

$$I_c\ddot{\psi}_c^r + k_{c\psi}\dot{\psi}_c^r + c_{c\psi}\psi_c^r = M_{sz} \quad (9.154)$$

and in addition equations for the residual deflections:

$$\dot{x}_c^r = V_{cx} - V_{b\xi} + r_e(\Omega - \dot{\theta}_b^r) \quad (9.155)$$

$$\dot{y}_c^r = V_{cy} - V_{b\eta} + r_l(\dot{\gamma} + \dot{\gamma}_b^r) \quad (9.156)$$

$$\dot{\psi}_c^r = \dot{\psi} - \dot{\psi} - \dot{\psi}_b^r \quad (9.157)$$

Also here, in the right-hand members, a road slope will have an effect. An axes transformation is needed to properly introduce the belt velocities with respect to the location of the contact patch. From the deflections and deflection rates the residual spring and damper forces appearing in Eqs.(9.146-151) can be determined. We have:

$$F_{cx} = k_{cx}\dot{x}_c^r + c_{cx}x_c^r \quad (9.158)$$

$$F_{cy} = k_{cy}\dot{y}_c^r + c_{cy}y_c^r \quad (9.159)$$

$$M_{cz} = k_{c\psi}\dot{\psi}_c^r + c_{c\psi}\psi_c^r \quad (9.160)$$

while

$$M_{cx} = M_{sx} \quad (9.161)$$

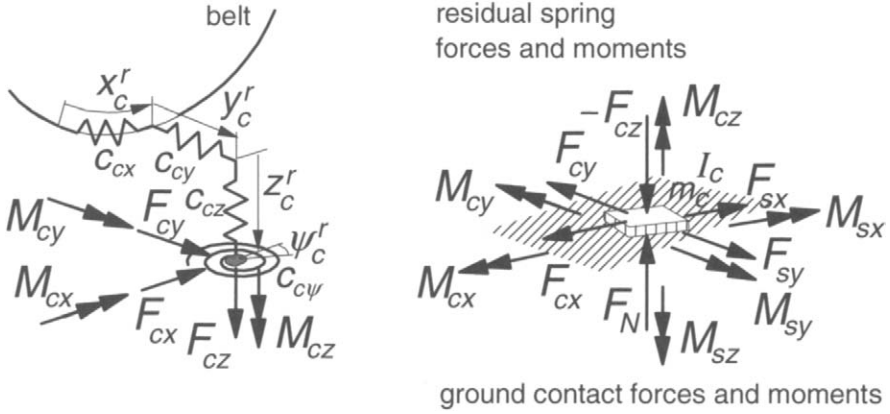


Fig. 9.28. Internal and external forces and moments acting on the contact patch body.

$$M_{cy} = M_{sy} \quad (9.162)$$

$$F_{cz} = F_{sz} \quad (9.163)$$

The contact forces and moments result from the contact slip model equations developed in the preceding section. The computed forces and moments have been defined according to the *Magic Formula* model which, at steady state, act with respect to the moving axes system (C, x, y, z). These forces and moments, here provided with subscript c , are to be transformed to arrive at the set of forces and moments defined according to the system with lines of action shifted sideways over the calculated 'static' lateral displacement y_{st}^r of the contact patch with respect to the wheel plane. These corrected quantities correspond to the forces and moments provided with subscript s occurring in the Eqs.(9.152-154) and (9.161-163).

$$F_{sx} = F_{x,C} \quad (9.164)$$

$$F_{sy} = F_{y,C} \quad (9.165)$$

$$M_{sz} = M_{z,C} + y_{st}^r \cdot F_{x,C} \quad (9.166)$$

$$M_{sx} = M_{x,C} - y_{st}^r \cdot F_{z,C} \quad (9.167)$$

$$M_{sy} = M_{y,C} \quad (9.168)$$

$$F_{sz} = F_{z,C} \quad (9.169)$$

where the static lateral deflection is computed from the side force and the overall lateral compliance of the standing tyre at ground level:

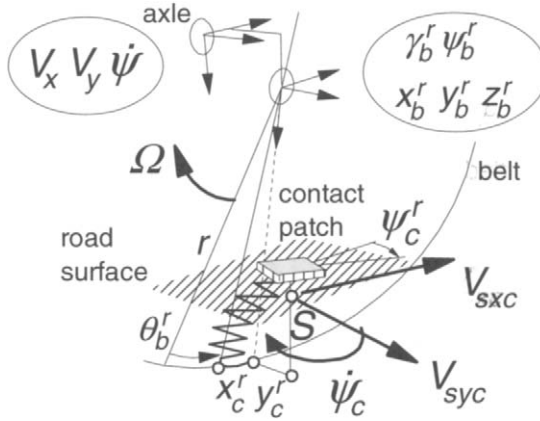


Fig. 9.29. Slip velocities of contact patch forming input to transient slip equations.

$$y_{st}^r = \frac{F_{sy}}{C_{Fy}} = F_{sy} \left(\frac{1}{c_{cy}} + \frac{1}{c_{by}} + \frac{r_l^2}{c_{b\gamma}} \right) \quad (9.170)$$

With the transient response variables computed with the aid of Eqs.(9.78-86) plus Eq.(9.20) the contact forces and moments may be found by using these variables as argument in the steady-state equations presented in Sections 4.3.2 and 4.3.3. We should, however, properly account for the response to a varying camber angle of the belt plane.

For this purpose, we introduce the tyre total spin velocity $\dot{\psi}_\gamma$, cf. Eq.(4.76) which has been corrected for the static belt camber deflection to enable the direct use of the relevant magic formulae (analogous to the use of β_{st} in Eq.(9.78)):

$$\dot{\psi}_\gamma = \dot{\psi}_c - (1 - \epsilon_\gamma) \Omega \sin(\gamma + \gamma_b^r - \gamma_{bst}^r) \quad (9.171)$$

with the 'static' belt deflection angle:

$$\gamma_{bst}^r = -r_l F_{sy} \frac{1}{c_{b\gamma}} \quad (9.172)$$

Further, we write instead of β_{st} :

$$\psi_{st}^r = M_{sz} \left(\frac{1}{c_{c\psi}} + \frac{1}{c_{b\psi}} \right) \quad (9.173)$$

The transient slip first-order differential equations are repeated below. They are identical to Eqs.(9.78-86) plus Eq.(9.20) except for the now added effect of the camber angle in the right-hand members. In (9.20) κ_c' may be replaced by κ' as at steady-state these are equal for contact patch and overall tyre model. The same holds for the spin variables φ_c' and φ' .

transient slip equations for longitudinal, side slip, turn slip and camber

$$\sigma_c \frac{d\kappa'}{dt} + |V_x| \kappa' = -V_{sxc} \quad (9.174)$$

$$\sigma_c \frac{d\alpha'}{dt} + |V_x| \alpha' = -V_{syc} - |V_x| \psi_{st}^r \quad (9.175)$$

$$\sigma_2 \frac{d\alpha'_t}{dt} + |V_x| \alpha'_t = |V_x| \alpha' \quad (9.176)$$

$$\sigma_c \frac{d\varphi'}{dt} + |V_x| \varphi' = -\dot{\psi}_\gamma \quad (9.177)$$

$$\sigma_{F2} \frac{d\varphi'_{F2}}{dt} + |V_x| \varphi'_{F2} = -\dot{\psi}_\gamma \quad (9.178)$$

$$\sigma_{\varphi 1} \frac{d\varphi'_1}{dt} + |V_x| \varphi'_1 = -\dot{\psi}_\gamma \quad (9.179)$$

$$\sigma_{\varphi 2} \frac{d\varphi'_2}{dt} + |V_x| \varphi'_2 = -\dot{\psi}_\gamma \quad (9.180)$$

In addition, we need the composite transient slip quantities:

$$\varphi'_F = 2\varphi' - \varphi'_{F2} \quad (9.181)$$

$$\varphi'_M = \varepsilon_\varphi^* \varphi' + \varepsilon_{\varphi 12} (\varphi'_1 - \varphi'_2) \quad (9.182)$$

The slip variables employed in the magic formulae (*MF*) are replaced by the transient slip variables as indicated in the arguments of the following expressions:

output forces and moments

$$F_{x,C} = MF_{F_x}(\kappa', \alpha', \varphi'_F, F_N) \quad (9.183)$$

$$F_{y,C} = MF_{F_y}(\kappa', \alpha', \varphi'_F, \gamma, F_N) \quad (9.184)$$

$$M_{z,C} = -t_C F_{y,C} + M_{zr,C} + s F_{x,C} + \Delta M_z \quad (9.185)$$

$$t_C = MF_t(\kappa', \alpha'_t, \varphi'_M, \gamma, F_N) \quad (9.186)$$

$$M_{zr,C} = MF_{M_{zr}}(\kappa', \alpha', \varphi'_M, \gamma, F_N) \quad (9.187)$$

$$\Delta M_z = C_{\Delta M}(\alpha' - \alpha'_t) \quad (9.188)$$

$$M_{x,C} = M_x \quad (9.189)$$

$$M_{y,C} = M_y \quad (9.190)$$

$$F_{z,C} = -F_N \quad (9.191)$$

Equation (9.188) has been added which is in agreement with the short wavelength transient slip theory, cf. Eqs.(9.106,9.110). The input to the transient slip equations (9.171,174-180) is constituted by the velocities of the contact patch, cf. Fig.9.29:

$$V_{sxc} = V_{cx} \quad (9.192)$$

$$V_{syc} = V_{cy} - V_x(\psi_b^r + \psi_c^r) \quad (9.193)$$

$$\dot{\psi}_c = \dot{\psi}_c \quad (9.194)$$

The overturning couple M_x can be modelled with the function (4.E69) where the F_y part may be replaced by the expression (4.122-124) with transient slip angle as argument, if the actual momentary loaded radius r_l (distance between points A and C) has been properly accounted for in the (steady-state) measurements and further processing. The wheel load $F_N (=|F_z|)$ and the rolling resistance moment M_y depend on the radial deflection and on a number of other variables. The subsequent section provides information on the experimentally assessed functional relationships.

Finally we need to establish the output forces and moments that act from the tyre upon and about the wheel centre. These quantities are denoted with the symbols K and T and are provided with the subscript a . The components are defined to act along and about the axes of the axle triad (A, ξ, η, ζ) . We find:

$$K_{a\xi} = K_{b\xi} \quad (9.195)$$

$$K_{a\eta} = K_{b\eta} \quad (9.196)$$

$$K_{a\zeta} = K_{b\zeta} \quad (9.197)$$

$$T_{a\xi} = T_{b\xi} + y_b^r K_{b\zeta} - z_b^r K_{b\eta} \quad (9.198)$$

$$T_{a\eta} = T_{b\eta} + z_b^r K_{b\xi} - x_b^r K_{b\zeta} \quad (9.199)$$

$$T_{a\zeta} = T_{b\zeta} + x_b^r K_{b\eta} - y_b^r K_{b\xi} \quad (9.200)$$

where the forces and moments acting from belt centre to rim are retrieved from Eqs.(9.131-136):

$$K_{b\xi} = k_{bx} \dot{x}_b^r + c_{bx} x_b^r + k_{bz} \Omega z_b^r \quad (9.201)$$

$$K_{b\eta} = k_{by} \dot{y}_b^r + c_{by} y_b^r \quad (9.202)$$

$$K_{b\zeta} = k_{bz} \dot{z}_b^r + c_{bz} z_b^r - k_{bx} \Omega x_b^r \quad (9.203)$$

$$T_{b\xi} = k_{b\gamma} \dot{\gamma}_b^r + c_{b\gamma} \gamma_b^r + k_{b\psi} \Omega \psi_b^r \quad (9.204)$$

$$T_{b\eta} = k_{b\theta} \dot{\theta}_b^r + c_{b\theta} \theta_b^r \quad (9.205)$$

$$T_{b\zeta} = k_{b\psi} \dot{\psi}_b^r + c_{b\psi} \psi_b^r - k_{b\gamma} \Omega \gamma_b^r \quad (9.206)$$

Values of inertia parameters normalised with tyre mass m_o and reference moment of inertia $m_o r_o^2$ with r_o the unloaded tyre radius have been listed in App.3.

9.3.2. Constitutive Relations

In the study of Zegelaar (1998) important observations have been made regarding contact area dimensions, static and dynamic vertical stiffness and characteristics at different speeds of rolling, static longitudinal stiffness of the standing tyre, tyre radius growth with speed, rolling resistance, effective rolling radius and rolling resistance couple. Much of the results will be repeated below.

Dimensions of the Contact Area

Prints of the contact patch may be obtained by using ink or carbon paper. The shape appears to change from an oval shape at very low normal loads to a more rectangular shape at higher values of the load. An effective rectangular contact area may be defined with an area equal to that of the envelope of the actual print. The ratio of the width and length of the rectangle is taken equal to that of the actual contact area. The effective half length and half width are denoted as a and b . The dimensions depend on the normal load $F_N (=|F_z|)$ and the following formulae have been found to give a good approximation:

$$a = (q_{a1} \sqrt{F_N/F_{No}} + q_{a2} F_N/F_{No}) r_o \quad (9.207)$$

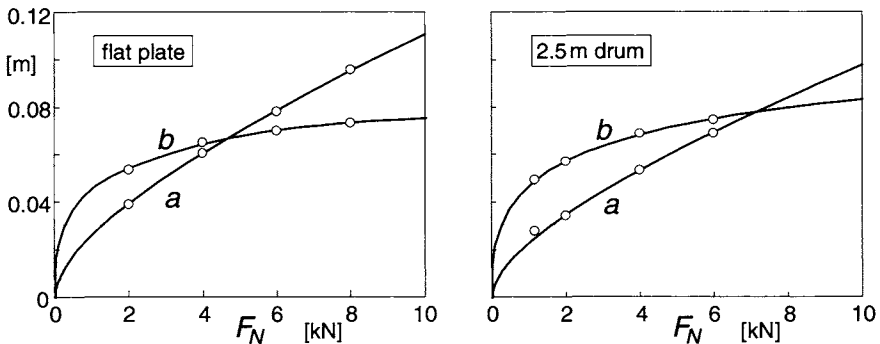


Fig. 9.30. Measured and calculated half length a and half width b of the contact patch vs wheel load, for the cases: loading on a flat plate and on a drum surface.

and

$$b = (q_{b1} \sqrt[3]{F_N/F_{No}} + q_{b2} F_N/F_{No}) r_o \quad (9.208)$$

with r_o denoting the free tyre radius. Figure 9.30 presents the curves compared with the measured effective quantities for the tyre pressed on a flat surface and on a curved drum surface with 2.5m diameter. Obviously, the results are satisfactory. The dimensions of the tyre were again: 205/60R15 91V at 2.2 bar inflation pressure. The non-dimensional parameter values can be found in Table 9.3. In App.3.3 an alternative expression for a is presented based on the radial deflection ρ_z instead of on the normal load F_N . The resulting value is much less dependent on the possibly changed inflation pressure, cf. Fig.A3.1.

Table 9.3. Parameter values for contact patch dimensions (205/60R15 91V at 2.2 bar).

$F_{No} (= F_{zo}) = 4000 \text{ N}, \quad r_o (=R_o) = 0.312 \text{ m}, \quad \text{drum diameter} = 2.5 \text{ m}$			
$q_{a1,\text{flat}} = 0.140$	$q_{a2,\text{flat}} = 0.053$	$q_{b1,\text{flat}} = 0.240$	$q_{b2,\text{flat}} = -0.037$
$q_{a1,\text{drum}} = 0.120$	$q_{a2,\text{drum}} = 0.050$	$q_{b1,\text{drum}} = 0.247$	$q_{b2,\text{drum}} = -0.027$

The Sidewall Stiffnesses and Damping

The rigid ring model of the tyre freely rolling and loaded on the road shows three in plane modes of vibration: the vertical mode and two angular modes. One of these rotational modes vibrates in phase with rim angular vibration while the other moves in anti-phase. The natural frequencies have been estimated with the aid of experiments conducted on the drum test stand where the wheel, at fixed axle position, rolls over a short cleat or is excited by brake torque fluctuations, cf. Sec.9.4.2.

The experiments indicate that the natural frequencies lying in the range of 0-100Hz, decrease with velocity. Other researchers found the same tendency, notably Bruni, Cheli and Resta (1996). Since the sidewall stiffnesses are much larger than the residual stiffnesses it is decided to make the in-plane sidewall stiffnesses dependent on the speed of rolling. As to the out-of-plane vibrations, Maurice did not ascertain the necessity to make the lateral, yaw and camber stiffnesses speed dependent.

Zegelaar introduces a variable quantity Q_v that is a measure of the time rate of change of the loaded tyre deformation due to rolling. We have the non-dimensional quantity (V_o representing the reference velocity, cf. Sec.4.3.2):

$$Q_v = \frac{|\Omega|}{V_o} \sqrt{(x_b^r)^2 + (z_b^r)^2} \quad (9.209)$$

The following expressions for the sidewall stiffnesses have been found to be appropriate:

$$c_{bx} = c_{bx0} (1 - q_{bVx} \sqrt{Q_V}) \quad (9.210)$$

$$c_{bz} = c_{bz0} (1 - q_{bVz} \sqrt{Q_V}) \quad (9.211)$$

$$c_{b\theta} = c_{b\theta 0} (1 - q_{bV\theta} \sqrt{Q_V}) \quad (9.212)$$

The additional subscript ₀ designates the situation of the loaded non-rotating tyre. The vertical and longitudinal stiffnesses have been assumed equal to each other. The parameters $q_{bVx,z,\theta}$ govern the speed dependency of the stiffnesses.

The sidewall damping coefficients $k_{bi} = k_{bx,y,z,\gamma,\theta,\psi}$ are considered to be constant quantities. The interaction terms appearing in Eqs.(9.131-136) containing the coefficients $k_{bi}\Omega$ are omitted since these terms affect the rolling resistance and the aligning torque (also in steady state) and would make these speed dependent. The introduction of material damping being inversely proportional with frequency would be closer to reality. Further on, the rolling resistance will be introduced in an alternative, better controlled way.

For the constant stiffnesses non-dimensional parameters may be introduced. We define with F_{No} , $r_o (=R_o)$ and m_o (the reference load, free tyre radius and tyre mass) the non-dimensional parameters q :

$$c_{bx0,y,z0} = q_{cbx,y,z} F_{No}/r_o \quad (9.213)$$

$$c_{b\gamma,\theta 0,\psi} = q_{cb\gamma,\theta,\psi} F_{No} r_o \quad (9.214)$$

$$k_{bx,y,z} = 2 q_{kbx,y,z} \sqrt{m_o F_{No}/r_o} \quad (9.215)$$

$$k_{b\gamma,\theta,\psi} = 2 q_{kb\gamma,\theta,\psi} \sqrt{m_o F_{No} r_o^3} \quad (9.216)$$

To provide more damping when the wheel speed gets close to zero, we may follow the theory of Chapter 7 and introduce $k_{V,low}$ as demonstrated in Chap.8, Eqs.(8.127,8.128) where the slip speed V_{sx} may be replaced V_{sxc} . In a similar way the residual stiffness and damping parameters c_c and k_c have been normalised.

The Normal Force

The spring with residual stiffness c_{cz} indicated in Fig.9.27 hides a structure that is a lot more complex than a spring with constant stiffness. Experiments reveal that the force deflection characteristics are non-linear: the force develops after contact has been made and increases slightly more than proportionally with the overall normal deflection ρ_z . Also, the tyre grows with speed due to the centrifugal action. Figure 9.31 illustrates both phenomena. Furthermore, it has been found useful to introduce F_x and F_y interaction terms in the vertical

stiffness, cf. Reimpell et al. (1986). The following formula is proposed for the normal force including interaction and overall stiffness and growth functions:

$$F_N = |F_z| = \left\{ 1 + q_{v2} |\Omega| \frac{r_o}{V_o} - \left(q_{Fcx1} \frac{F_x}{F_{No}} \right)^2 - \left(q_{Fcy1} \frac{F_y}{F_{No}} \right)^2 \right\} \left((q_{Fz1} + q_{Fz3} \gamma^2) \frac{\rho_z}{r_o} + q_{Fz2} \frac{\rho_z^2}{r_o^2} \right) F_{No} \quad (9.217)$$

With radius r_c of assumed circular cross section contour, the deflection becomes at wheel camber angle γ (relative to normal to road plane), also cf. Eq.(7.46):

$$\rho_z = \max((r_o - r_l + \Delta r) \cos \gamma + r_c (1 - \cos \gamma), 0) \quad (9.218)$$

The tyre radial growth changes quadratically with rotational velocity:

$$\Delta r = q_{v1} r_o (\Omega r_o / V_o)^2 \quad (9.219)$$

Here, r_o denotes the radius of the free non-rotating tyre, r_l the loaded radius (distance between wheel centre and contact centre) and Δr the increase in free tyre radius due to wheel rotation velocity. The non-dimensional parameter q_{v1} governs the influence of tyre growth, q_{v2} the stiffness variation with speed, $q_{Fcx,y1}$ the interaction with horizontal forces and $q_{Fz1,2,3}$ the stiffness and non-linearity of the force deflection characteristic at zero speed and zero horizontal forces. Appendix 3 presents the parameter values fitted to experimental data. To radically simplify (9.218) take $r_c = r_o - r_l + \Delta r$ being equal to the radial deflection.

From the overall characteristics the properties of the residual spring are to be derived. An exact functional relationship may be established but it can be found that the residual normal spring characteristic can be approximated by the third degree polynomial function:

$$F_N = |F_z| = a_1 \rho_{zr} + a_2 \rho_{zr}^2 + a_3 \rho_{zr}^3 \quad (9.220)$$

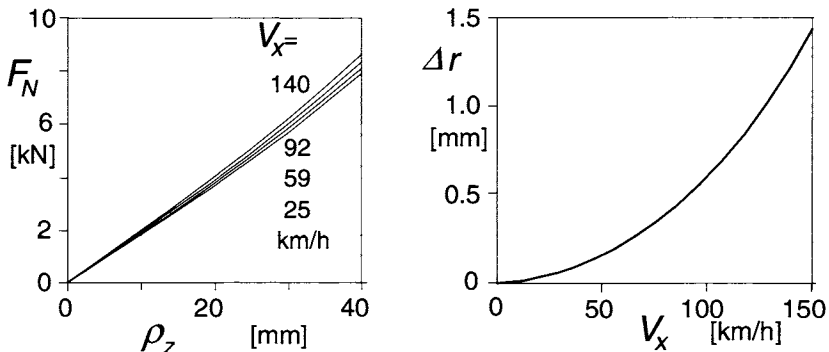


Fig. 9.31. Vertical load vs normal deflection characteristics at various forward velocities and tyre radius growth with speed.

with the F_N related normal residual spring deflection (taking into account geometrical interaction terms with horizontal deflections):

$$\rho_{zr} = \rho_z + z_b^r \cos \gamma - q_{Fcx2} \rho_x^2 / r_o - q_{Fcy2} \rho_y^2 / r_o \quad (9.221)$$

Here, z_b^r is the radial displacement of the centre of the belt ring with respect to the wheel centre and $\rho_{x,y}$ represent the longitudinal and lateral tyre contact deflections. The actual loaded radius r_l results from the calculated deflections (cf. Fig.4.30 for measured evidence) with camber influence included:

$$r_l = r_o + z_b^r + \Delta r + \{r_c(1 - \cos \gamma) - \rho_{zr} - (q_{Fcx2} \rho_x^2 + q_{Fcy2} \rho_y^2) / r_o\} / \cos \gamma \quad (9.222)$$

The coefficients appearing in (9.220) can be expressed in terms of sidewall stiffness c_{bz} and wheel speed of revolution Ω :

$$a_1 = \frac{c_{bz} A_1}{c_{bz} - A_1} \quad (9.223)$$

$$a_2 = \frac{c_{bz}^3 A_2}{(c_{bz} - A_1)^3} \quad (9.224)$$

$$a_3 = 2 \frac{c_{bz}^4 A_2^2}{(c_{bz} - A_1)^5} \quad (9.225)$$

where with Reimpell's terms in (9.217) omitted, we obtain:

$$A_1 = (q_{Fz1} + q_{Fz3} \gamma^2)(1 + q_{v2} |\Omega| r_o / V_o) F_{No} / r_o \quad (9.226)$$

$$A_2 = q_{Fz2} A_1 / \{(q_{Fz1} + q_{Fz3} \gamma^2) r_o\} \quad (9.227)$$

where the non-dimensional parameters q_{v2} and $q_{Fz1,2,3}$ of Eq.(9.217) appear. The horizontal tyre deflections at road surface level with respect to the wheel rim are (at small camber):

$$\rho_x = x_b^r + r_o \theta_b^r + x_c^r \quad (9.228)$$

$$\rho_y = y_b^r - r_o \gamma_b^r + y_c^r \quad (9.229)$$

Appendix 3 provides the relevant parameter values for the passenger car tyre that has been tested.

Free Rolling Resistance

Experiments show that the rolling resistance force F_r (pointing backwards) is proportional to the tyre normal load F_N . A history on this subject can be found in the publication of Clark (1982). We have:

$$F_r = f_r F_N \quad (9.230)$$

The rolling resistance coefficient f_r depends on the forward speed and may be expressed in terms of powers of the speed, cf. Mitschke (1982):

$$f_r = q_{sy1} + q_{sy3}|V_x/V_o| + q_{sy4}(V_x/V_o)^4 \quad (9.231)$$

Parameter q_{sy1} governs the initial level of the rolling resistance force and typically lies in between 1 and 2 %. Parameter q_{sy3} controls the slight slope of the resistance with speed. The last parameter q_{sy4} represents the sharp rise of the resistance that occurs after a relatively high critical speed is surpassed. Then, the so-called standing waves show up as a result of instability, cf. Pacejka (1981), or according to an alternative theory due to resonance, cf. Brockman and Braisted (1994). The formation of standing waves gives rise to large deflection variations and considerable energy loss. The phenomenon may result in failure of the tyre and poses an upper limit to the safe range of operation of the tyre.

Below, we will see that the rolling resistance will be introduced in the tyre model through the rolling resistance moment that is imposed on the tyre belt ring as an external torque about the y axis, cf. Eq.(9.236).

Effective Rolling Radius, Brake Lever Arm, Rolling Resistance Moment

In Chapter 8 the notion of the effective rolling radius has been introduced. Figure 8.12 shows the results of experiments of tyres running over a drum surface. In Subsection 8.3.1 the theory is restricted to a linearised representation of the variation of the effective rolling radius with radial deflection. The complete non-linear variation versus normal load F_N may be described by the expression:

$$r_e = r_o + \Delta r - \{q_{re1}\rho_z + D_{re} \arctan(B_{re}\rho_z)\} \quad (9.232)$$

with

$$D_{re} = q_{re2}F_{No}/C_{Fz} \quad (9.232a)$$

$$B_{re} = q_{re3}/D_{re}$$

and the vertical stiffness of the standing tyre at nominal load F_{No} as derived from Eq.(9.217):

$$C_{Fz} = \frac{F_{No}}{r_o} \sqrt{q_{Fz1}^2 + 4q_{Fz2}} \quad (9.232b)$$

The longitudinal slip velocity is defined with r_e introduced as the slip radius, cf. e.g. Eq.(8.32). Note the slightly deviating formula in App.3, Eq.(A3.7).

In the present model with the belt ring and contact patch modelled as separate bodies, the longitudinal slip velocity V_{sxc} of the contact patch is used as input in the transient slip differential equation (9.174). In Eq.(9.192) with

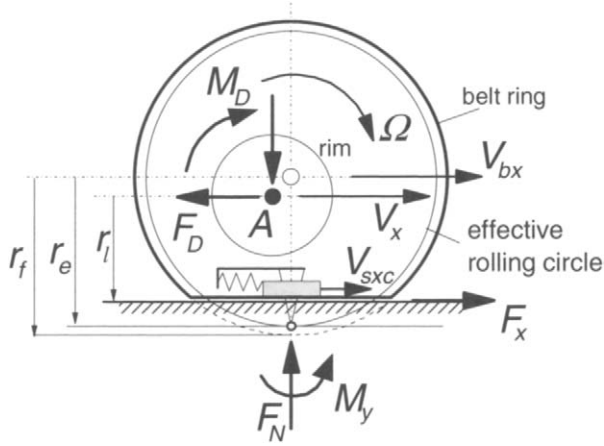


Fig. 9.32. The driven tyre-wheel combination with deflected belt and residual spring.

(9.155) the effective rolling radius r_e accomplishes the transmission of the rotational speed of the belt to the residual deflection rate of change. At steady-state condition, the deflection rates vanish and we have the following relation for the longitudinal slip speed:

$$V_{sx} = V_x - r_e \Omega \quad (9.233)$$

We may consider the power balance of a wheel subjected to a propulsion torque M_D and a drag force F_D acting backwards on the wheel in its centre. Figure 9.32 depicts the situation. The connected power flow diagram is presented in Fig. 9.33. The S represents a power source (the engine) and the R's are resistors where energy is dissipated. The balance of power requires that the equation holds:

$$M_D \Omega = F_D V_x + M_y \Omega - F_x V_{sx} \quad (9.234)$$

or with (9.233):

$$M_D - M_y = F_x r_e \quad (9.235)$$

This suggests, at least for the model employed, that the moment arm equals the

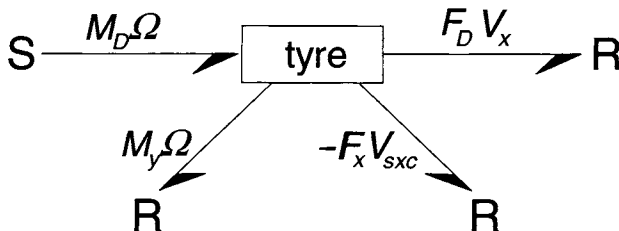


Fig. 9.33. Power flow diagram (bond graph) of driven tyre wheel combination in steady state.

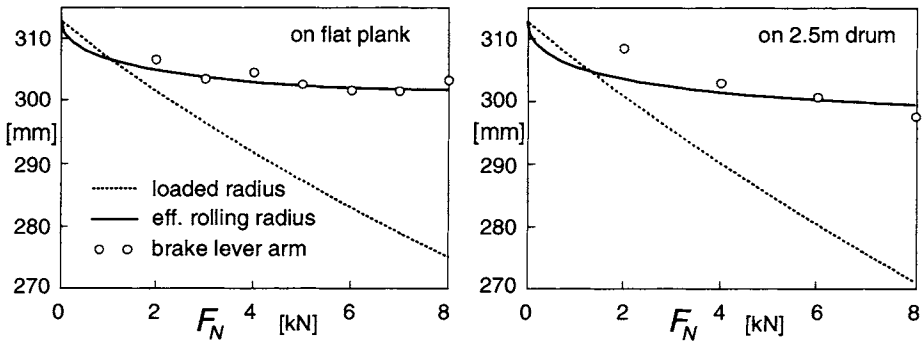


Fig. 9.34. Tyre radii as function of the normal load measured at zero or very low speed.

effective rolling radius (defined at zero driving or braking torque: free rolling). Consequently, the block named 'tyre' in the diagram of Fig.9.33 represents, when unfolding the bond graph, a junction structure containing a transformer with modulus r_e that transforms the angular speed into (a part of) the slip speed and, in opposite direction, the slip force into the drive torque.

Experiments have been carried out by Zegelaar on both the flat plank machine and the drum test stand to establish the effective rolling radius and the moment arm. In these tests a brake torque was applied to the wheel. The moment arm may be termed as the brake lever arm. The diagrams of Fig.9.34 have been obtained from tests performed at zero (brake lever arm) and very low speed of travel (effective rolling radius). Especially in case of the flat surface an excellent agreement has been found to occur. It is assumed that the growth of the effective rolling radius with speed is equal to that of the free tyre radius, cf. Eq.(9.219).

The diagrams of Fig.9.35 present the influence of speed on the two radii. The

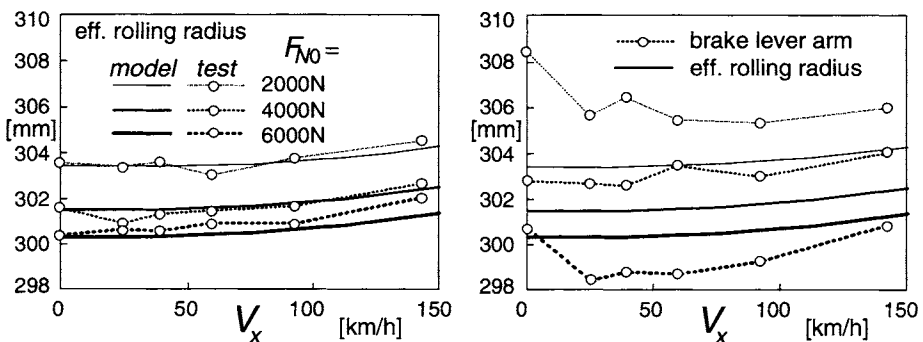


Fig. 9.35. Tyre radii measured on 2.5m drum as a function of the forward speed at three axle heights corresponding to the indicated initial loads. Average level and amplitude of brake torque are small.

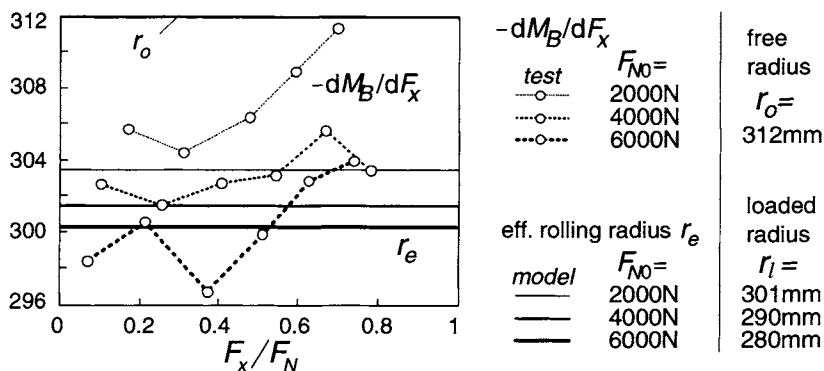


Fig. 9.36. Ratio of brake torque increment to brake force increment as function of level of brake force at a velocity of 25km/h and three different axle heights (loaded radii).

loaded radius has been kept fixed so that the vertical load rises when the speed is increased. Three different axle heights have been selected corresponding to the indicated initial vertical loads at zero speed F_{N0} . The left-hand diagram shows the degree of fit for the effective rolling radius. The right-hand diagram shows the correspondence with the brake lever arm. The tests from which the brake lever arm can be assessed have been conducted at low levels of the average and the standard deviation of the brake torque random input (120 and 22Nm respectively). The brake lever arm results from the longitudinal force response to the imposed brake torque variation at zero frequency. The influence of the average brake torque on the ratio of the torque amplitude and the force amplitude at zero frequency, $-dM_B/dF_x$ is given in Fig.9.36. This ratio does not appear to be a constant. Especially at low loads and relatively large braking forces large deviations arise from the value of the effective rolling radius. Obviously, due to its definition, the effective radius is not affected by the magnitude of the brake force.

With the effective radius adopted as the brake or driving torque moment arm the rolling resistance moment becomes (acting about C-y axis):

$$M_y = F_x(r_e - r_l) + F_r r_l \cdot \arctan(V_r/V_o) \quad (9.236)$$

which also contains the free rolling resistance moment $F_r r_l$ according to Eq.(9.230) and the arctan function to take care of a possible sign change of the wheel rolling speed.

In Appendix 3 a complete set of parameter values has been listed for both the *Magic Formula* model and the *SWIFT* model.

9.4. Dynamic Tyre Model Performance

A number of experiments has been conducted at the Delft University of Technology to assess the parameters of the dynamic model and to judge its performance. The steady-state side slip, longitudinal slip and camber force and moment characteristics have been typically assessed from over the road experiments with the Delft Tyre Test Trailer. For the model performance evaluation, steady-state characteristics have been used, obtained from tests carried out on the drum with the strain gauge equipped measuring hub mounted in the measuring tower, cf. Fig.9.37.

In Section 9.4.1 the dedicated dynamic test facilities have been indicated, followed by Section 9.4.2 with the presentation of the model dynamic behaviour in comparison with experimental data. In Chapter 10 the model will be extended to include the description of running over road obstacles (cleats). This model extension is followed by the presentation of experimental results compared with model behaviour.

The reader is referred to Chapter 12 for a more extensive description of steady-state and higher frequency test facilities including the dedicated rigs mentioned in the section below. For some practical details regarding parameter assessment for advanced dynamic tyre models Section 10.2 may be of interest. In this context, it is important to note that cleat tests are most useful to determine both the in-plane and the out-of-plane natural frequencies of the model. Also modal testing of the unloaded tyre with fixed wheel axle may provide useful, possibly additional, information.

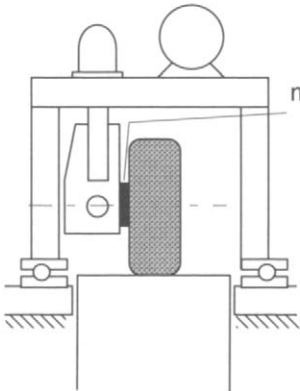
9.4.1. Dedicated Dynamic Test Facilities

Dynamic Brake and Cleat Test Rig

Experiments have been conducted on the 2.5 m steel drum test stand provided with a specially designed rig equipped with a disc brake installation, cf. Fig.9.37 and for more details: Chapter 12, Fig.12.6. Brake torque fluctuation tests (Sec. 9.4.2) and dynamic cleat tests (Sec.9.5.5) have been carried out. The test facilities with numerous experimental and simulation results have been described in detail by Zegelaar (1998).

The wheel axle height can be adjusted to select the tyre initial load. During the tests the axle position is held fixed causing the wheel load to rise with

measuring tower



dynamic brake and cleat test stand

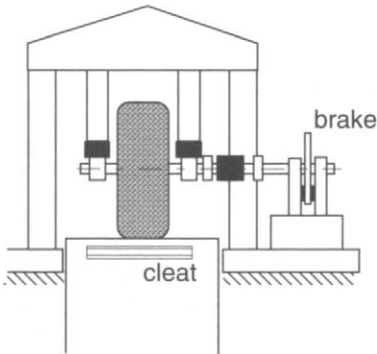


Fig. 9.37. Principle setup of the measuring tower and of the dynamic brake and cleat test stand.

increasing speed. The wheel axle bearing supports are equipped with piezo electric load cells. Steady-state or average force levels can not be measured very well with these force transducers. To provide an indication of the actual load increase with speed as measured in the measurement tower equipped with a hub provided with strain gauges, Table 9.4 gives for a series of initial deflections (ρ_{z0} at zero speed) the values of the average vertical force derived from measurements at different speeds. The values have been obtained from Eqs.(9.217-219) after having fitted the parameters involved. The loads shown apply for the cases of nominal loads 2000, 4000, 6000N indicated in the graphs presented in the next section.

Table 9.4. Vertical load on 2.5m drum at constant axle height and increasing speed (tyre: 205/60R15 91V at 2.2 bar)

V_x [km/h]	initial vertical deflection ρ_{z0} [mm]			
0	0	11.90	22.57	32.33
	vertical load F_N [N] at constant axle height			
0	0	2115	4153	6133
25	7	2166	4246	6288
39	17	2202	4307	6352
59	40	2264	4404	6483
92	100	2388	4588	6727
143	249	2642	4939	7169

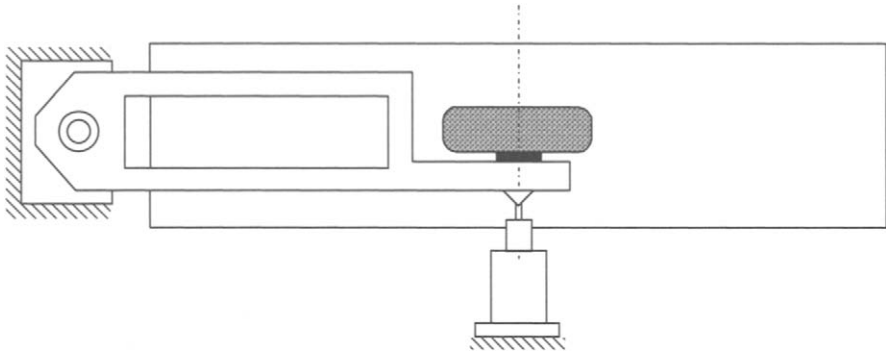


Fig. 9.38. Principle sketch of the trailing arm 'pendulum' test rig exciting the tyre almost purely laterally. Frequencies up to ca. 25 Hz, adequate for assessing the tyre relaxation length and gyroscopic coupling parameter.

Pendulum and Yaw Oscillation Test Rigs

To assess the lateral and yaw tyre dynamic parameters two test rigs have been developed. One is the trailing arm 'pendulum' test stand with at one end a vertical hinge and at the other the steering head with piezo-electric measuring hub. At that point the arm is excited laterally up to ca. 25 Hz through a hydraulic actuator. Cf. Fig.9.38 and for more details: Chapter 12, Fig.12.7. The rig is useful to assess the overall relaxation length and the gyroscopic couple coefficient, both needed for the simpler transient models treated in Chapter 7. The idea of the pendulum concept originates from Bandel et al. (1989). They designed and used an actual pendulum rig. The natural frequency of the freely swinging trailing arm with tyre rolling on the drum was taken to establish the

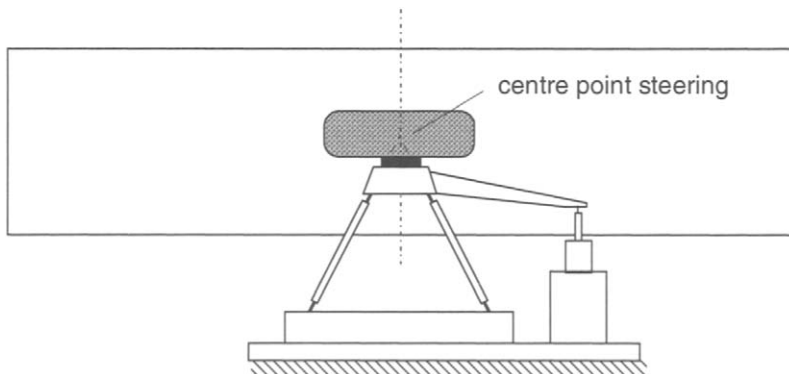


Fig. 9.39. Principle sketch of the yaw oscillation test rig featuring centre point steering. Frequencies up to ca. 65 Hz enabling the assessment of tyre out-of-plane inertia and stiffness parameters including residual stiffnesses and rigid modes.

relaxation length σ . This quantity is the parameter of the first-order differential equation such as used in Chapter 7. Bandel found that σ increases with speed. However, when using a model in which a belt ring with mass is used, it turns out that the parameters can be kept constant, cf. Vries and Pacejka (1998b). Consequently, tyre inertia, notably the gyroscopic couples, give rise to the speed dependency of the effective relaxation length.

Another rig was developed to investigate the response of the tyre subjected to yaw oscillations at frequencies up to ca. 65 Hz. The structure depicted in Fig.9.39 is light and very stiff, also see Fig.12.8. The two guiding members with flexible hinges intersect in the vertical virtual steering axis that is positioned in the wheel centre plane (centre point steering). A hydraulic actuator is mounted to generate the yaw vibration. The wheel axle is provided with a piezo-electric measuring hub. The tyre is loaded by adjusting the axle height above the drum surface. During the test the loaded radius remains constant.

The measuring tower, cf. Fig.9.37, provided with a hydraulic vertical axle positioning installation is used to conduct pure braking and pure side slip tests as well as combined slip experiments at axle height oscillations and radial dynamic stiffness tests up to ca. 15 Hz.

A detailed description of the various side slip test facilities together with a full account on the numerous experiments conducted and the simulation results of the model have been given by Maurice (2000) and for motorcycle tyres by Vries and Pacejka (1998a,b).

9.4.2. Dynamic Tyre Simulation and Experimental Results

In general, the values of the model parameters can be estimated by minimizing the difference between measured and calculated frequency response functions (both amplitude and phase). In some cases (in particular the in-plane response) special aspects of the response functions may be considered to successfully assist the parameter assessment process. These aspects are: the position and width of resonance peaks (sidewall and residual stiffnesses and damping), the phase relationship in the low frequency range (overall relaxation length which itself is not a parameter!), the yaw response at zero speed (yaw residual stiffness). The residual damping ratios have been chosen equal to those of the sidewalls. Another help is the establishment of the inertia parameters of the relevant part of the tyre by cutting the tyre into pieces and considering the parameters of these parts. Rolling over a cleat might be used to estimate some of the parameters but the most accurate way is the identification through frequency response functions. These are obtained with the aid of the random brake test with the measured brake

torque (or the measured wheel speed) used as input, the yaw oscillation test and the vertical axle oscillation test.

Vibrational Modes

The vibrational modes of the tyre may be assessed through modal analysis of the tyre wheel system with axle fixed and tyre loaded and/or unloaded. When comparing these results with calculated modes using the parameter values assessed by means of the frequency response functions of the rolling tyre, it is found that the stiffnesses found from the dynamic rolling experiments are ca. 30% lower than those estimated from experimental modal analysis, cf. Zegelaar. These differences must be due to the different operational conditions and the larger amplitudes of the vibrations and higher temperatures that occur in the realistic rolling experiments.

The calculated vibrational rigid body modes at zero speed using the parameters as established from experiments carried out on the drum have been depicted in Figs. 9.40 and 9.41.

We have four in-plane degrees of freedom of belt ring and wheel rim (two translational and two rotational) and three out-of-plane degrees of freedom (lateral, yaw and camber). As a consequence, we can distinguish four in-plane rigid modes and three out-of-plane rigid body modes. The mode shapes change considerably when the tyre is making contact to the drum surface. The free rotation (0 Hz) mode changes into a mode with the belt and rim rotating in phase with respect to each other. The lateral and camber modes appear to form combinations: one low frequency mode with a low axis of camber oscillations and one high frequency mode with a rotation axis closer to the top of the tyre and relatively large lateral deflections in the contact zone. The yaw mode in the loaded case shows a higher calculated natural frequency since the effect of turn slip has been included which was not the case in Maurice's original model. This means that the yaw stiffness of the contact tread has now been accounted for.

The natural frequencies n and damping ratio ζ change with the speed of rolling. In Table 9.5 the values have been presented for the loaded tyre running at a velocity of 0 and 30 m/s. Especially the out-of-plane modes show considerable changes in frequency and damping. The camber and yaw mode natural frequencies which are identical in the unloaded zero speed case, exhibit a with speed growing mutual difference with the camber mode frequency becoming smaller and the yaw mode frequency larger.

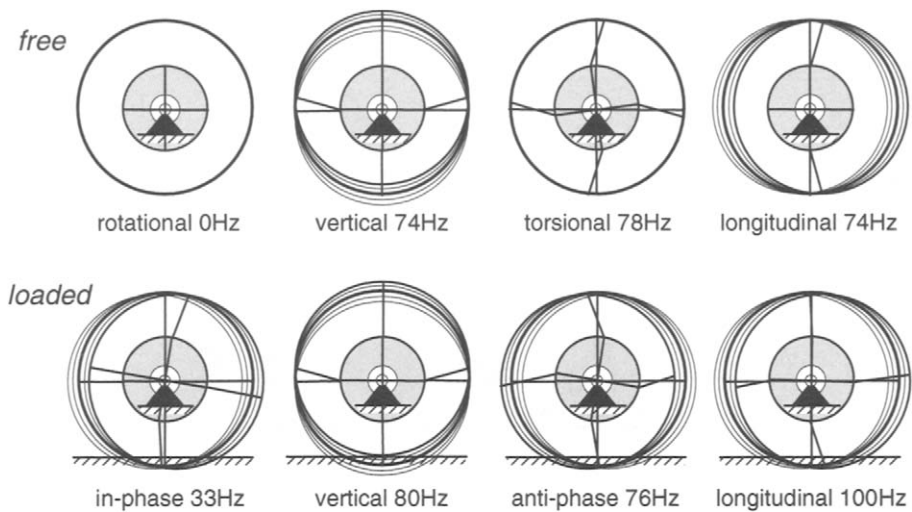


Fig. 9.40. Calculated in-plane vibrational modes of tyre/wheel system with axle fixed and tyre free or loaded on the drum surface with vertical load $F_N = 4000\text{N}$ and at zero speed.

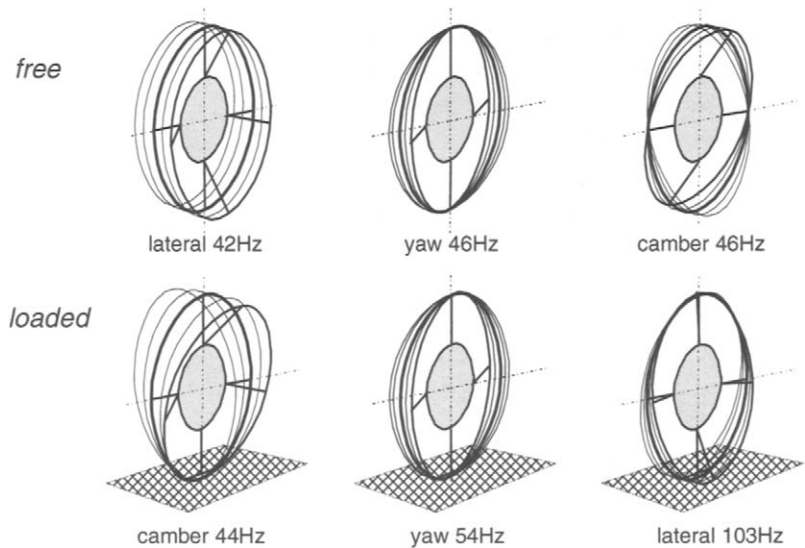


Fig. 9.41. Calculated out-of-plane vibrational modes of tyre/wheel system with axle fixed and tyre free or loaded on the drum surface with vertical load $F_N = 4000\text{N}$ and zero speed.

Table 9.5. Natural frequencies and damping of vibrational modes of rigid ring tyre model calculated at a vertical load $F_N = 4000\text{N}$ for two values of forward speed

forward speed [m/s]	0	30	0	30
	n [Hz]		ζ [%]	
<i>in-plane modes</i>				
in-phase	33	30	0.10	0.25
vertical	80	75	0.05	0.05
anti-phase	76	71	0.05	0.05
longitudinal	100	129	0.77	0.35
<i>out-of-plane modes</i>				
camber	44	33	0.03	0.05
yaw	54	51	0.03	0.04
lateral	103	101	0.01	0.24

Frequency Response Functions

A typical example of measured and calculated in-plane frequency response functions has been depicted in Fig.9.42. Coherence functions show that the tests give sensible results up to ca. 80 Hz. Similar response functions have been obtained by Kobiki et al. (1990). The left-hand diagram of the figure represents the response function of the longitudinal force $F_x (=K_{\alpha_x}$ in Eq.(9.195)) acting on the wheel axle to the imposed brake torque variation considered to be applied in the torque meter. The right-hand diagram shows the response of the force to wheel slip variations. The wheel slip is derived from the measured wheel and drum speeds.

The two peaks occurring in the left-hand diagram belong to the in-phase and the anti-phase modes. The single peak showing up in the right-hand diagram belongs to the mode that would arise if the rim is fixed also in rotation. The natural frequency lies in between the frequencies of the peaks in the left diagram. The natural frequencies contribute to assess the sidewall stiffnesses. From the right-hand diagram two quantities can be derived: the slip stiffness and the overall relaxation length. Through the latter, additional information is obtained to find the fore and aft residual stiffness. From careful interpretation of the frequency response functions assessed at different speeds, the sidewall stiffness dependence on the speed of rolling has been ascertained. Resulting calculated

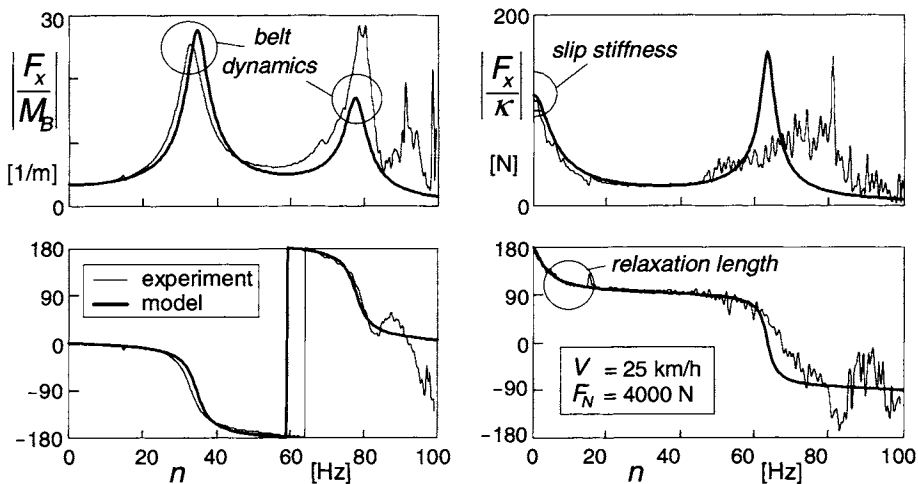


Fig. 9.42. Measured and calculated in-plane frequency response functions at an average braking force of 450N and assessed at a braking force standard deviation of 75N.

response functions at different loads and brake torque level gave satisfactory agreement with measured behaviour. We refer to the original work of Zegelaar (1998) for detailed information.

The out-of-plane frequency response functions of the side force $F_y (=K_{ay})$ and the aligning torque $M_z (=T_{az})$ to yaw oscillations have been presented in Figs. 9.42,43. The parameters have been assessed by minimising the difference between measured and calculated (complex) response functions. The correspondence achieved between measured and computed curves at different speeds, loads and side slip level is quite satisfactory, cf. Maurice (2000) for more details. To conduct a proper comparison, the measured data have been corrected for the inertia of the wheel and part of the tyre that moves with the wheel. The expected splitting up of the single peak at low velocity into two peaks, one belonging to the camber mode and the other to the yaw mode, and the growing difference of the two natural frequencies with increasing speed is clearly demonstrated. This phenomenon which is due to the gyroscopic action, has already been observed to occur with the stretched string model with inertia included approximately, cf. Fig.5.40. It is noted that the theoretical results of Maurice have been established by using the model that did not include the equations for the response to spin (9.177-180). Especially the aligning moment is sensitive to turn slip. The moment response curves to side slip and yaw of the massless tyre model as depicted in Fig.9.16 are quite different. The dip in the moment amplitude response curve to yaw oscillations occurring in the curve for M_ψ in Fig.9.16 does not appear in the curve for the response to side slip

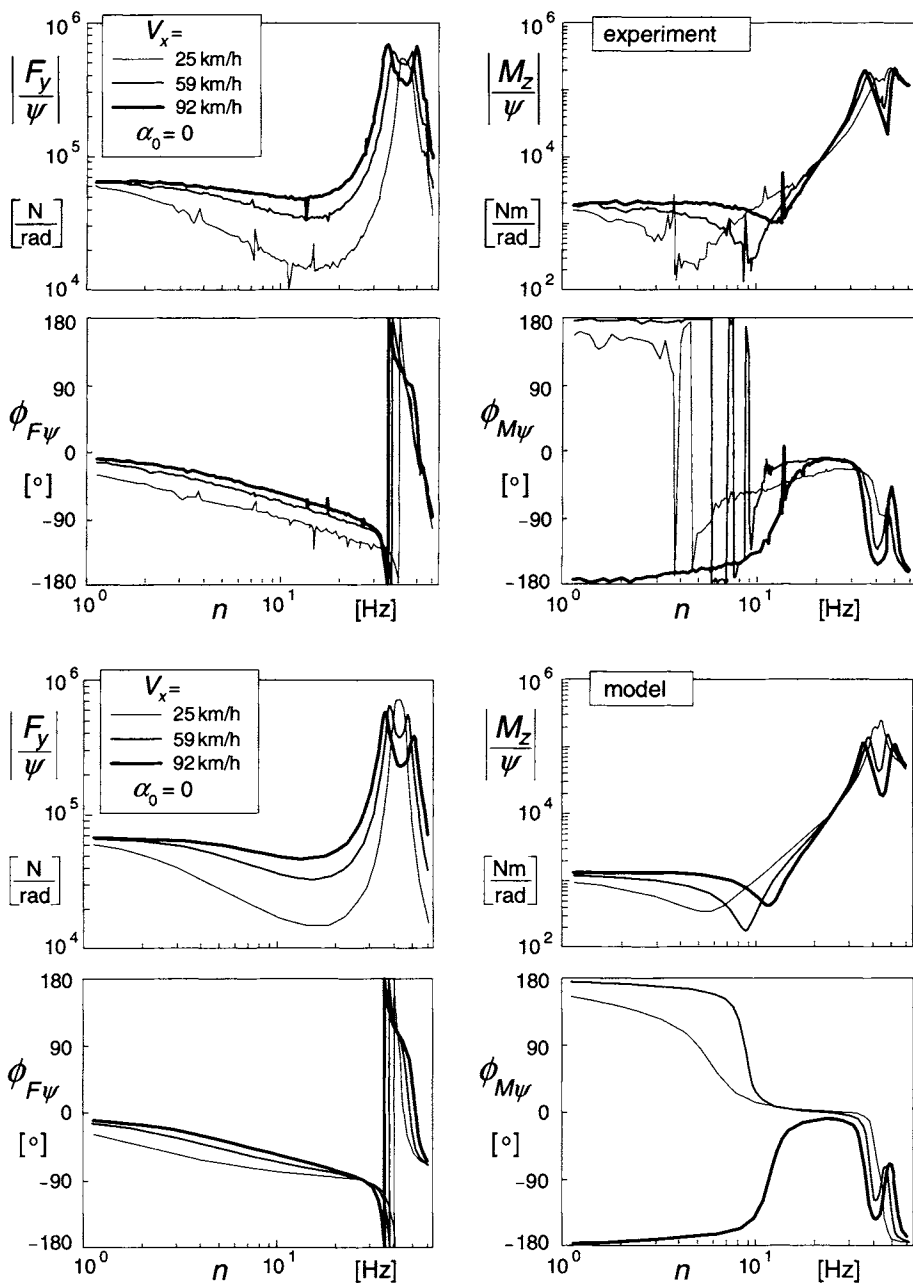


Fig. 9.43. Measured and calculated out-of-plane frequency response functions of the side force and aligning torque to steer angle variations at zero average slip angle for three values of forward speed and normal load $F_N = 4000$ N.

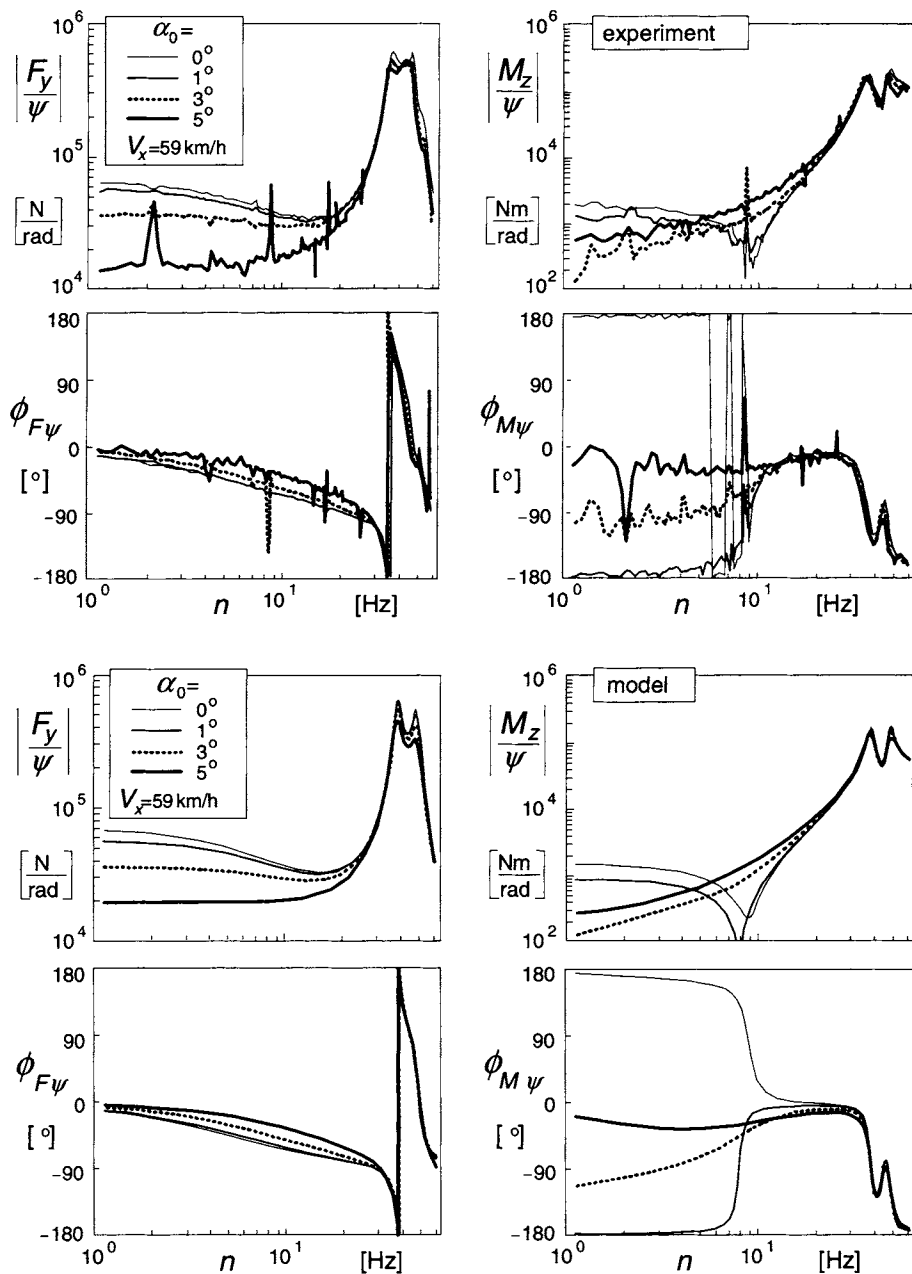


Fig. 9.44. Measured and calculated out-of-plane frequency response functions of the side force and aligning torque to steer angle variations at one value of speed and at four levels of average side slip and wheel load $F_N = 4000\text{N}$.

M_a . This dip also appears in the curves of Fig.5.40 where spin is included as well. It is surprising to see that a similar dip occurs in the Figs.9.43,9.44. The minimum arises here due to the tendency of the response to side slip to decrease and tend to zero at increasing path frequency while at the same time the moment amplitude increases due to tyre inertia when approaching the resonance peak. The dip in the measured curve of the upper right-hand diagram of Fig.9.43 at 25km/h is deeper than the one shown by the theoretical curve of the lower diagram. This may be due to the additional action of spin in the actual tyre. As shown by both the theoretical and measured curves of Fig.9.44 the dip disappears altogether at larger average side slip.

The experiments conducted with the trailing arm 'pendulum' test rig where the tyre is subjected to almost pure side slip and the spin is very small, also show satisfactory correspondence with model behaviour (Maurice 2000; also: De Vries and Pacejka, motorcycle tyres, 1998b). This also appears to hold for a limited number of conducted combined slip tests and the response to vertical axle motions at side slip and braking carried out with the measuring tower.

Apparently, the rigid ring model provided with the short wavelength transient slip model is very well capable of describing the dynamic tyre behaviour in the frequency range up to about 60 Hz. Furthermore, it may be concluded that the spin part is only necessary when dealing with short wavelength, especially low speed phenomena where tyre inertia is less important, such as with parking.

Time Domain Responses

To demonstrate the performance of the model, simulations and experiments have been carried out pertaining to successive stepwise increases in brake pressure and steer angle.

The response of the longitudinal force and the associated wheel speed has been presented in Fig.9.45. The lower diagram clearly depicts the oscillatory variation of the force vs slip ratio. The measured response shows a faster decay of the wheel velocity after the highest brake effort has been reached. Apparently, this is due to the friction coefficient being lower in the experiment than assumed in the model. Finally, the brake is released and the wheel spins up again. The oscillations (ca. 28Hz) correspond to the in-phase vibrational mode of the system with the brake disc/axle inertia included.

Figure 9.46 shows the responses to successive changes in steer angle for both the side force and the aligning torque at a given load and speed. The responses clearly show vibrations attributed to the yaw/camber mode with natural frequency of ca. 40Hz (cf. Fig.9.43, 25 km/h). Also, the decrease of the overall relaxation length at larger slip angle can be recognized.

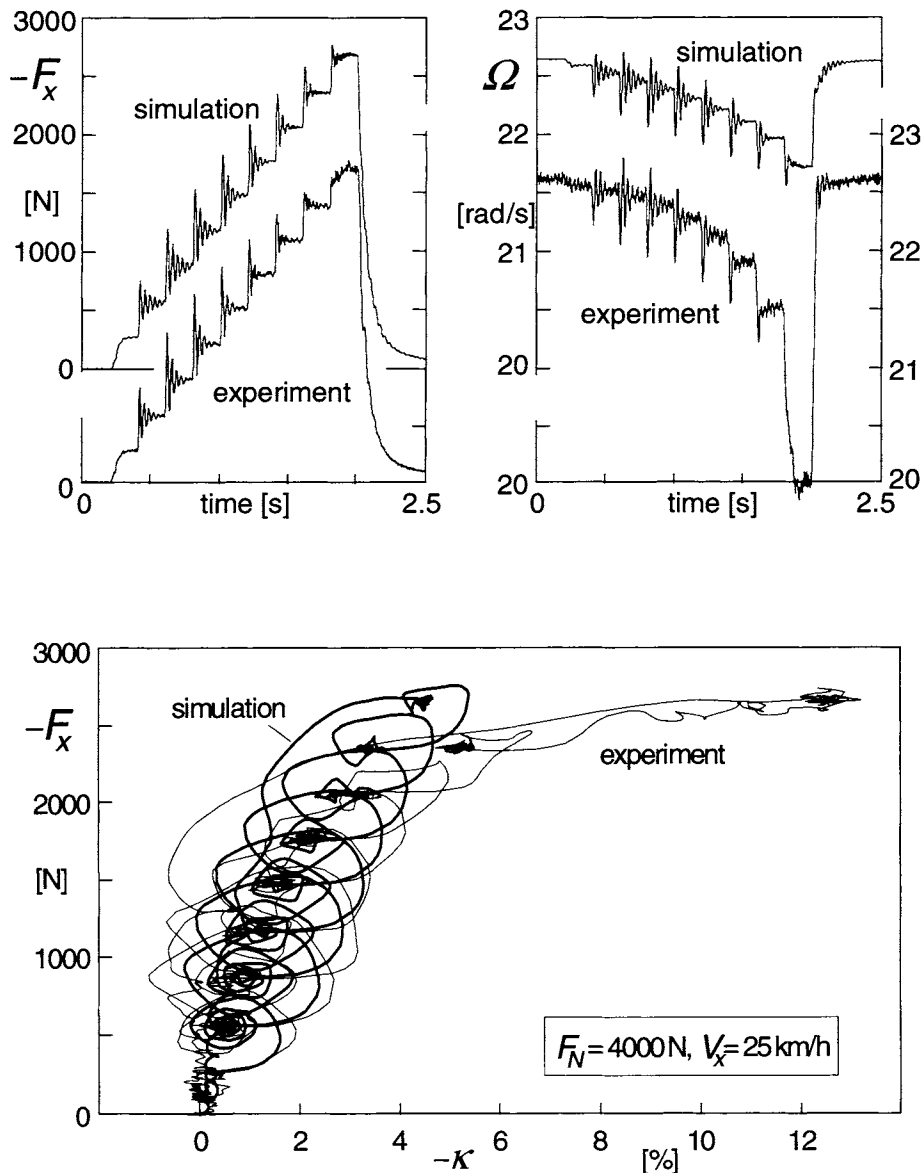


Fig. 9.45. Brake force response to successive step increments of brake pressure. The upper diagrams depict the variation of force and wheel speed of revolution with time. The lower figure shows the loops in the force vs wheel slip diagram. Apparently, the actual friction coefficient is lower than assumed in the model. (Zegelaar 1998).

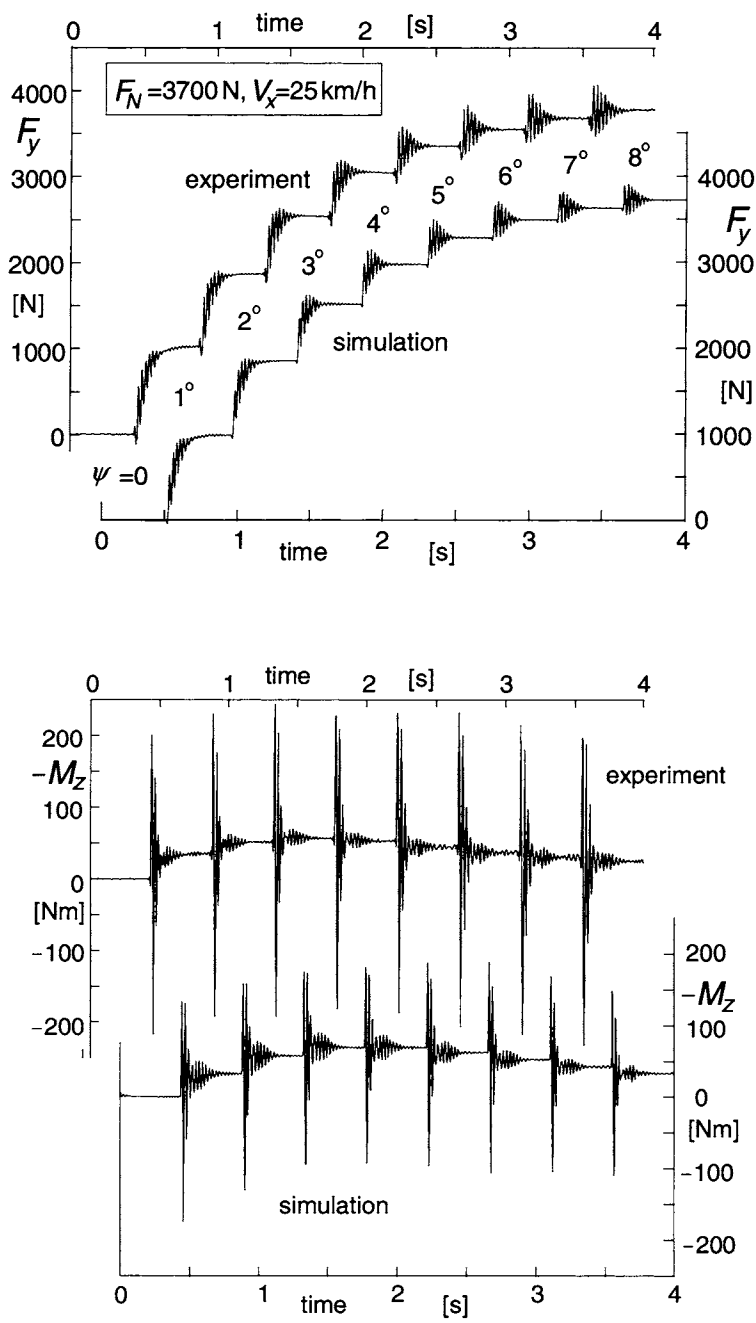


Fig. 9.46. Side force and aligning torque response to successive step changes in steer angle. (Maurice 2000)